

Decay of hot, high-spin nuclei produced in  ${}^6\text{Li}$ -induced fusion reactionsS. E. Vigdor, H. J. Karwowski,\* W. W. Jacobs, S. Kailas,† P. P. Singh,  
F. Soga,‡ and T. G. Throwe*Indiana University Cyclotron Facility, Bloomington, Indiana 47405*

(Received 19 March 1982)

The decay of compound nuclei formed at high excitation and angular momentum in  ${}^6\text{Li}$  bombardment of  ${}^{181}\text{Ta}$ ,  ${}^{194,198}\text{Pt}$ ,  ${}^{197}\text{Au}$ , and  ${}^{208}\text{Pb}$  has been investigated in a coherent program of experiments and statistical model analysis. The measured decay properties include absolute cross sections for fusion and for all major competing decay modes, fission-fragment angular distributions, charged-particle energy spectra, and  $({}^6\text{Li}, xn)$  residue mass distributions. The measurements are compared with highly constrained calculations in which all nuclear structure parameters are fixed to values consistent with the rotating-liquid-drop and noninteracting Fermi-gas models. Possible ambiguities in interpreting the experimental results, and the likely influence of neglected effects on the statistical model calculations, are explored. In order to obtain good quantitative agreement with all measurements it is necessary to simulate in the calculations the effects of preequilibrium nucleon emission in the early stages of the decay, and it is furthermore helpful to allow the collective enhancements of deformed-nucleus level densities to fade out with increasing temperature. Within existing uncertainties in the statistical model treatment, reproduction of the experimental results does not require any appreciable macroscopic or microscopic corrections to the nuclear structure input parameters. Several experimental methods for studying more selectively the fission and particle decay of low-excitation, high-spin nuclei, and thereby enhancing sensitivity to microscopic structure contributions, are suggested.

NUCLEAR REACTIONS Fusion, fission, particle emission for  ${}^6\text{Li} + {}^{181}\text{Ta}$ ,  ${}^{194,198}\text{Pt}$ ,  ${}^{197}\text{Au}$ ,  ${}^{208}\text{Pb}$ ,  $E({}^6\text{Li}) = 74.8, 84.2, 94.4$  MeV; measured energy spectra,  $\sigma_{\text{tot}}$ ,  $\sigma(\theta)$  for fission and inclusive charged-particle emission,  $\sigma_{\text{tot}}$  and mass distribution of residual nuclides for  $({}^6\text{Li}, xn)$  reactions; compared measurements with statistical model calculations incorporating simple macroscopic structure predictions, deformed-nucleus level densities, "hot-spot" simulation of preequilibrium nucleon emission; discussed theoretical uncertainties in statistical model analysis, possibilities for experiments with enhanced sensitivity to microscopic structure.

## I. INTRODUCTION

Much of the current interest in the structure of nuclei at high spin stems from the expectation of dramatic shape changes with the addition of angular momentum. At the simplest level the evolution in shape can be predicted on the basis of the classical rotating-liquid-drop model (RLDM, Ref. 1), in which the potential energy surface (PES) of the nucleus as a function of deformation and spin ( $J$ ) is determined by the balance among macroscopic surface, Coulomb, and rotational energy contributions. One expects the RLDM predictions for high-spin structure to be modified significantly in a real nu-

cleus by the inclusion of explicit single-particle degrees of freedom—by allowing for generation of angular momentum from alignment of single-particle spins as well as from collective rotations, and by correcting the PES for shell and pairing effects which themselves depend on deformation and spin.<sup>2,3</sup> The investigation and understanding of the interplay between these macroscopic and microscopic aspects of high-spin nuclear structure are the goals of a wide variety of current experimental and theoretical research.

It is of particular interest to study the variation with angular momentum of the energy and shape for both the yrast state (corresponding to the

minimum in the PES) and the saddle-point state (the lowest fission-unstable maximum in the PES) of a nucleus. According to the RLDM, both of these energies should increase with increasing  $J$ , but the difference between them—i.e., the fission barrier height  $B_{\text{fiss}}(J)$ —should decrease monotonically, and eventually vanish with increasing angular momentum.<sup>1</sup> Considerable progress has been made in probing the yrast line of selected nuclei via experimental investigations of the  $\gamma$ -decay cascades in (heavy ion,  $xn$ ) residues.<sup>4</sup> In contrast, previous attempts to extract quantitative information about  $B_{\text{fiss}}(J)$  from studies of the fission and particle decay of high-spin nuclei have led to questionable and conflicting conclusions<sup>5–14</sup> and have stimulated the more complete and systematic investigation reported here.

In both the present and previous experiments, the decaying nuclei studied have been produced, unavoidably at high excitation energy ( $E^*$ , or temperature  $\tau$ ) as well as over a broad range of  $J$  values, in heavy-ion induced fusion reactions. As illustrated in Fig. 1, particle or fission decay may then occur from the compound nucleus (CN) directly or at any subsequent stage in the decay chain by which the system “cools” to excitation energies below the particle emission and fission thresholds. From observations which are integrated over the decay chain, one may hope to extract information about  $B_{\text{fiss}}(J)$  and the  $s$ -wave particle separation energies  $B_v(J)$  only by some sort of statistical model unfolding of the competition among the many open decay channels.<sup>6–9</sup> This statistical competition is unfortunately quite sensitive to many poorly understood aspects of the nuclear structure and fusion reaction mechanism, over and above the spin and deformation dependence of the CN potential energy surface, in which we are ultimately interested. For example, it depends crucially on nuclear level densities and their variation with neutron and proton number, spin, shape, and excitation energy; on (Coulomb plus centrifugal) barrier penetrabilities for particle decay from highly excited and possibly strongly deformed nuclei; on the initial spin distribution in the CN; on the path by which thermal equilibrium among the intrinsic nuclear degrees of freedom is reached, and the relative time scales for this equilibration versus the observed decay.

The difficulty in adequately constraining such statistical model analyses, usually compounded by experimental ambiguities in determining the cross sections for formation and decay of the CN, is reflected in the diversity of conclusions reached about high-spin structure in previous investigations.<sup>5–15</sup>

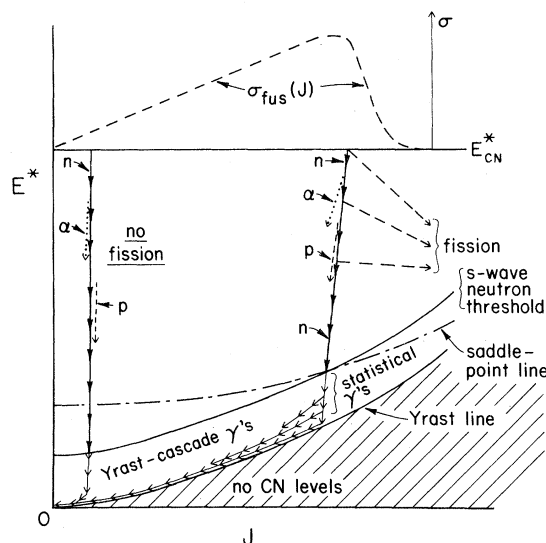


FIG. 1. Schematic illustration of possible decay modes of a compound nucleus (CN) formed at a unique high excitation energy  $E_{\text{CN}}^*$  and over a broad range of spins  $J$ , with population cross section  $\sigma_{\text{fus}}(J)$ . The decay chains indicated for low and high spins are intended to illustrate that evaporation of a given type of particle or (for high  $J$ ) fission may occur at various stages in the deexcitation process. The competition among different decay modes is sensitive to the  $p$ ,  $n$ , and  $\alpha$ -particle binding energies and barrier penetrabilities, the fission barrier heights, the level densities at yrast and saddle-point deformations, and the CN spin distribution.

For example, Beckerman and Blann<sup>6</sup> are able to fit fission excitation functions for CN in the mass range  $100 \leq A \leq 180$  only by using high-spin fission barrier heights which are consistently 50–60% of the values expected from the RLDM.<sup>1</sup> From analysis of similar measurements for a different compound system in the same mass region, Plasil *et al.*<sup>12</sup> conclude that the fission barriers are closer to 80% of the RLDM values. Delagrangé *et al.*<sup>7</sup> use barrier heights which are generally *larger* than the RLDM values to fit fission data for  $A_{\text{CN}} \approx 190$ , and also require very much larger level densities at the saddle-point deformation than were needed in the above analyses. Faber and Ploszajczak<sup>15</sup> argue that even the qualitative features of the decay of  $^{194}\text{Hg}$  from high spin and excitation can be understood only if one incorporates sizable spin-dependent shell corrections to the particle separation energies and fission barriers, which were not explicitly included in any of the statistical model analyses. The results of other work<sup>9–11,13,14</sup> in similar mass regions tend to add to the confusion.

In this paper we report the results of a coherent program of measurements and statistical model calculations aimed at determining whether one can, in fact, learn *anything* quantitatively about high-spin nuclear structure by studying the decay of hot fusion products. In order to constrain the analysis of the CN decay much more effectively than in previous work,<sup>5–14</sup> we have had to significantly expand the scope and improve the techniques of both the experiment and the calculations. We have measured a wide variety of observables characterizing the CN decay in reactions induced by  ${}^6\text{Li}$  on  ${}^{181}\text{Ta}$ ,<sup>194,198</sup>  ${}^{197}\text{Pt}$ ,  ${}^{197}\text{Au}$ , and  ${}^{208}\text{Pb}$ , each at bombarding energies of 74.8, 84.2, and 94.4 MeV. The grazing angular momentum for these projectile-target combinations is typically 45–50  $\hbar$ , while our measurements of fusion cross sections suggest (see Secs. III and IV B) that only for  $J \lesssim 30$ –35  $\hbar$  are completely fused compound nuclei formed. (In this mass and spin region, the RLDM predicts<sup>1</sup> mildly oblate yrast and strongly prolate saddle-point deformations, and fission barrier heights comparable to neutron separation energies.) The CN excitation energies are in the range 70–100 MeV, corresponding to temperatures  $\sim 1.7$ –2.1 MeV.

For each case studied we have compared measurements and statistical model calculations for a number of quantities, among them the absolute total cross sections for *all* of the major competitive CN decay modes: fission ( $\sigma_{\text{fiss}}$ ),  $\alpha$ -particle evaporation ( $\sigma_{\alpha}$ ),  $Z=1$  particle evaporation ( $\sigma_{Z=1}$ ), and multiple neutron emission ( $\sigma_{xn}$ ). With the measurement techniques used (to be detailed in Sec. II) these cross sections represent mutually exclusive processes, and their sum provides an experimental value of the total cross section for CN formation:

$$\sigma_{\text{fus}} = \sigma_{\text{fiss}} + \sigma_{\alpha} + \sigma_{Z=1} + \sigma_{xn} . \quad (1)$$

(While measurement of  $\sigma_{\text{fus}}$  is essential to constrain the initial CN spin distribution, one should keep in mind that the definition of  $\sigma_{\text{fus}}$  is somewhat subjective.<sup>16–18</sup> There is no sharp distinction between composite systems which decay *subsequent to*, and those which decay *during*, the attainment of thermal equilibrium.) We have also measured and calculated the angular distribution  $W_{\text{fiss}}(\theta)$  of the fission fragments, the backward-angle energy spectra of the emitted charged particles, and, in selected cases, the distribution of ( ${}^6\text{Li}, xn$ ) residues. We have thus generated a data set far more complete and systematic than has been subjected to previous statistical model analyses.<sup>5–14</sup> The target dependence of the cross sections is especially relevant in delineating the influence of nuclear structure on the

competition between decay modes: The compound nuclei studied ( ${}^{187}\text{Os}$ ,  ${}^{200,204}\text{Tl}$ ,  ${}^{203}\text{Pb}$ , and  ${}^{214}\text{At}$ ) span a wide range in expected shell corrections and ground-state shapes (e.g., see Ref. 2), and an appreciable range in expected saddle-point shapes.<sup>1</sup>

We have also substantially expanded the scope of the statistical model calculations in comparison with most previous work, e.g., by including a calculation of  $W_{\text{fiss}}(\theta)$  (Refs. 19–21), an improved treatment of level densities for deformed nuclei,<sup>22,23</sup> and a facility for simulating the effects of preequilibrium particle emission on subsequent evaporation and fission. Even with these improvements and the present expanded data set, however, the analysis is still not sufficiently constrained that we may deduce meaningful structure information in an unbiased fashion, by allowing all of the many (often hidden) parameters involved to vary freely to fit the measurements. In such an approach we should have to parametrize, for example, the dependences on  $N$ ,  $Z$ ,  $J$ , and  $E^*$  of the particle separation energies and of the yrast and saddle-point energies, moments of inertia, and level density parameters.<sup>24</sup> In reality we know that all these structure parameters are not mutually independent: The spin dependence of the energies and the moments of inertia are clearly closely allied; shell and pairing corrections affect all of the structure, in correlated ways.<sup>19,25,26</sup> Given the complexity of the problem, it is crucial that the structure input to a calculation be self-consistent and incorporate the expected correlations. This is best guaranteed by *fixing* the input according to *predictions* of a selected structure model—i.e., by including microscopic corrections, within some chosen prescription, for *all* of the relevant nuclear structure, *or none* of it. In this way we view the measurements of decay properties as providing, at best, an experimental test of various structure models.

At the moment there are no sufficiently complete Strutinsky-type microscopic calculations,<sup>2,3</sup> including predictions of both deformation energy surfaces and level densities over the entire relevant range of  $N$ ,  $Z$ ,  $J$ ,  $E^*$ , and nuclear shape, on which to base structure input for our statistical model calculations. Our analysis to date has thus treated the nucleus as a two-component noninteracting Fermi gas (NIFG) with an overall shape and (zero-temperature) deformation energy given by the RLDM. We have included some collective enhancement of deformed-nucleus level densities,<sup>22,23</sup> but *completely omitted* microscopic corrections (even to nuclear masses, as required by our self-consistency constraint). This is an eminently

reasonable starting point for the analysis since microscopic structure predictions evolve toward these macroscopic limits at moderately high temperatures (where shell and pairing effects wash out).<sup>25,27</sup> There are, of course, other parameters involved in the statistical model analysis than those which describe the nuclear structure, e.g., the inverse reaction cross sections (i.e., barrier penetrabilities) for particle emission, and the CN spin distribution; in most of our calculations we have also fixed these to conform with what we deem to be the best available information from other sources (details will be given in Sec. IV B).

Given our restriction so far to a single, very simple, macroscopic nuclear structure model, what can we hope to learn from the comparison of theory and experiment? We can first of all check whether the average decay properties are, in fact, consistent with RLDM-NIFG and the assumption of decay from a thermally equilibrated nucleus. It is important in this context to identify the ambiguities which exist in the statistical model treatment *within* the confines of the above assumptions, and to estimate the associated level of uncertainty in the present calculations. If systematic discrepancies exceeding this uncertainty are observed, we can try to discern whether they reflect inadequacies in the structure model, in the equilibrium assumption, or in some other aspect of the input parameters. In particular, we can look for evidence (especially in the comparison of measured and predicted target dependences) regarding the necessity for including microscopic structure corrections to obtain a quantitative understanding of the decay. We can vary parameters, not in an attempt to fit the measurements, but to explore the sensitivities of the various measured quantities. On this basis we can devise more selective second-generation experiments with enhanced sensitivity to particular interesting aspects of the interplay between macroscopic and microscopic contributions to high-spin structure.

Brief reports of various aspects of this work,<sup>21,28</sup> and a review of the results and relevant theoretical background,<sup>29</sup> have been published previously. The present report is organized as follows: The experimental techniques used and various characteristics of the measurements, along with possible ambiguities in their interpretation, are discussed in Sec. II. The experimental results are presented in Sec. III. In Sec. IV we describe the statistical model analysis, with emphasis on the basis for our input parameter choices and the sensitivity of the calculations to various parameters. [The central assumptions underlying the analysis, and some of our major im-

provements to the code MB-II (Ref. 30), are discussed in the following paper.<sup>23</sup>] The measurements are compared in Sec. V with fixed-parameter calculations based on the assumption of pure equilibrium decay of the CN, and with other calculations incorporating a simulation of some preequilibrium effects. The conclusions of the present work are summarized in Sec. VI. There we suggest several future experimental approaches to study more selectively the fission and particle decay of *low*-excitation, high-spin nuclei, and thereby to enhance sensitivity to microscopic structure contributions in comparison with the present investigation.

## II. MEASUREMENTS

### A. Charged-particle detection

All of the measurements were made using  ${}^6\text{Li}^{+++}$  beams obtained from the Indiana University Cyclotron Facility. For the fission and charged-particle evaporation measurements beams with typical intensities of 50–150 nA (electrical) bombarded self-supporting metallic foils mounted in a 163-cm diameter scattering chamber. The  ${}^{194,198}\text{Pt}$  and  ${}^{208}\text{Pb}$  targets were isotopically enriched to >95%. The target thicknesses were in the range 1.8–2.2 mg/cm<sup>2</sup>, except for  ${}^{208}\text{Pb}$  (4.9 mg/cm<sup>2</sup>) and for a thinner  ${}^{197}\text{Au}$  target (0.80 mg/cm<sup>2</sup>) used in some runs to cross-check the fission data obtained with the thicker (2.15 mg/cm<sup>2</sup>)  ${}^{197}\text{Au}$  target.

Full energy spectra for all emitted charged particles from protons through fission fragments were acquired simultaneously using a five-element silicon-detector telescope, with a front counter thickness of 12  $\mu\text{m}$ , a total depth of 12 mm, and a solid angle of 0.3 msr. The representative two-dimensional spectra ( $E_{\text{total}}$  vs  $\Delta E$ ) shown in Fig. 2 demonstrate the broad dynamic range of this telescope and the very clean separation obtained (over the full angular range  $10^\circ \leq \theta_{\text{lab}} \leq 170^\circ$ ) between fission fragments and all other reaction products. This clear distinction of the fragments is characteristic of fission induced by relatively light ions, since there are no significant deeply inelastic (or “quasifission”) processes involving massive transfer to the projectile, which might be confused with fission. In the present paper, we confine our attention to results for the  $Z = 1$ ,  $Z = 2$ , and fission groups in Fig. 2. Energy spectra and angular distributions for these groups will be discussed separately below.

The yields measured in the telescope were normalized via the sum of  ${}^6\text{Li}$  elastic scattering events

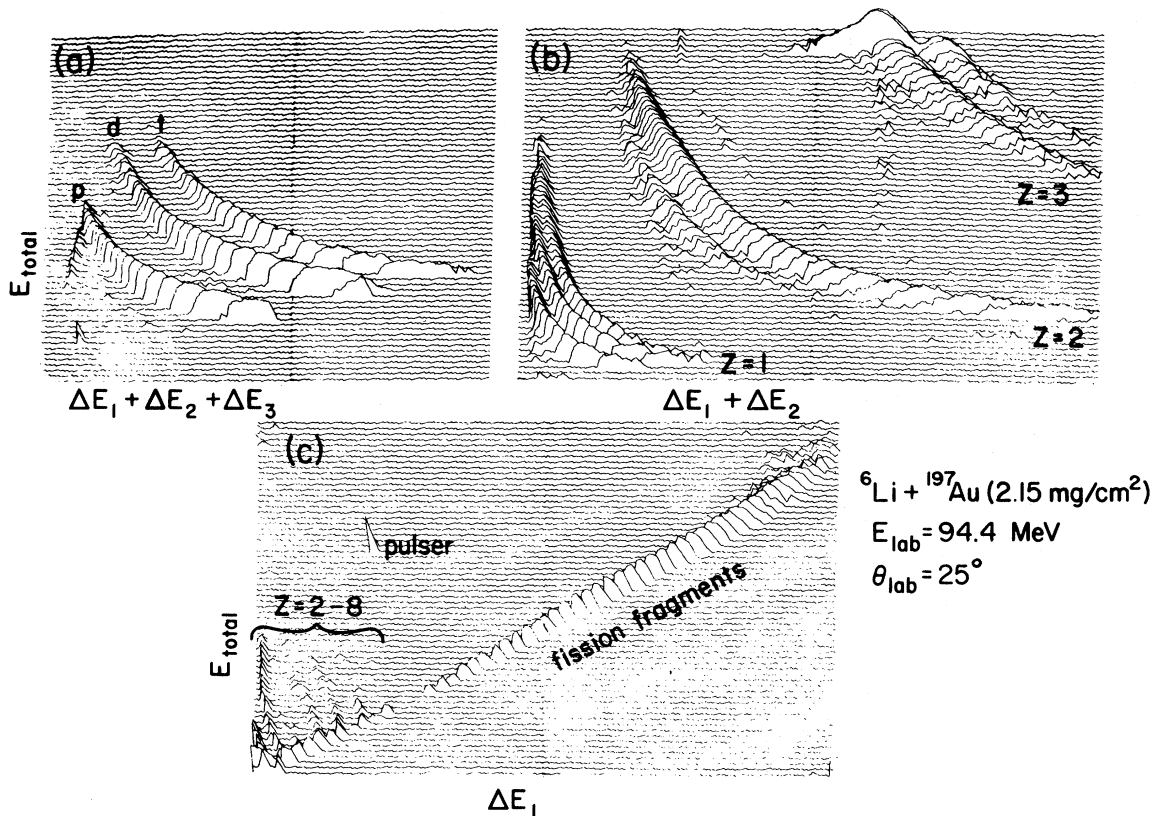


FIG. 2. Representative two-dimensional spectra obtained with the five-element charged-particle telescope. The plots show  $E_{\text{total}}$  vs (a)  $(\Delta E_1 + \Delta E_2 + \Delta E_3)$  for particles which reach at least the fourth detector in the stack, (b)  $(\Delta E_1 + \Delta E_2)$  for particles which reach at least the third detector, and (c)  $\Delta E_1$  for those particles which stop in the first or second detector. The calibration of the  $E_{\text{total}}$  scale is the same in all three plots. The vertical (counts) scale is logarithmic. Full energy spectra for  $p$ ,  $d$ , and  $t$  are reconstructed cleanly with the use of all three plots, with the lowest-energy portion obtained by expanding the  $\Delta E_1$  gain considerably in comparison with that used in (c). Energy straggling in the target contributes significantly to the observed breadth of the fission group in (c).

collected simultaneously in two silicon monitor detectors placed symmetrically to the left and right of the beam direction at  $\theta_{\text{lab}} = (10.0 \pm 0.04)^\circ$ . Absolute cross sections were obtained, using geometric measurements of the ratio of telescope and monitor-detector solid angles, under the assumption that the  $10^\circ$  elastic differential cross section is purely Rutherford for all the targets studied at  $E_{\text{lab}} = 74.8$  MeV. This assumption is confirmed to an accuracy of  $\pm 2\%$  by optical model calculations employing parameters deduced in an investigation<sup>31</sup> of 99-MeV  ${}^6\text{Li}$  scattering from  ${}^{208}\text{Pb}$ . At the higher bombarding energies the monitor cross sections were determined relative to those at 74.8 MeV using the same targets and Faraday-cup beam integration; the results for all targets were within 5% of Rutherford at 84.2 MeV and within 8% at 94.4 MeV.

The overall normalization uncertainty for absolute charged-particle cross sections reported in this paper is  $\pm 5\%$  at 74.8 MeV and  $\pm 6-7\%$  (depending on the target) at the higher energies.

The ratio of counts in the left versus right monitor detectors was used to correct the nominal telescope angle settings for the sometimes sizable shifts in incident beam direction. By this technique we obtained typically  $\pm 0.1^\circ$  accuracy in the relative telescope angle. There may be an additional absolute angle shift (affecting all measurements) of  $\sim \pm 0.1^\circ$ . Corrections to the telescope yields for electronic and computer-processing dead times were measured with a pulser triggered by the monitors, fed into the telescope-detector preamplifiers, and processed in a manner similar to the pulses from the detected particles.

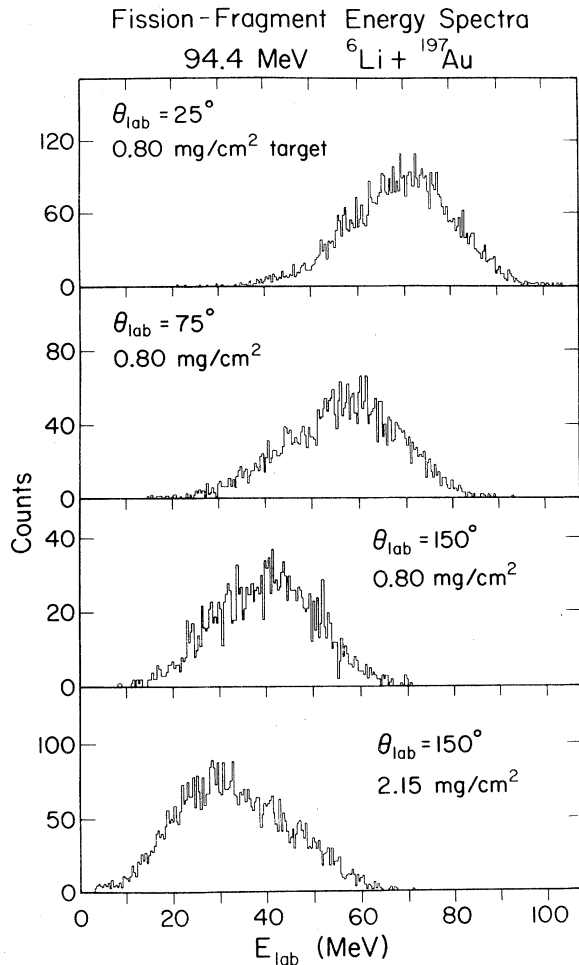


FIG. 3. Fission-fragment energy spectra obtained at several angles for 94.4-MeV  ${}^6\text{Li} + {}^{197}\text{Au}$ . The two spectra shown for  $150^\circ$  differ because of the increased energy loss and straggling of the fragments in the thicker ( $2.15 \text{ mg/cm}^2$ ) Au target.

### B. Fission characteristics

Fission-fragment energy spectra obtained at several angles for 94.4-MeV  ${}^6\text{Li} + {}^{197}\text{Au}$  are shown in Fig. 3. After approximate correction for energy loss in the target and for pulse height defect in the detector,<sup>32</sup> the observed centroid energies in Fig. 3 are consistent with well established fission-fragment kinetic energy systematics.<sup>33</sup> Because the spectra at all angles are free from contamination by any other reaction products, the accuracy of the measured fission cross section was not at all reduced in going from the  $0.80$  to the  $2.15 \text{ mg/cm}^2$   ${}^{197}\text{Au}$  target, despite the substantial increase in the energy loss

and straggling of the fragments (compare spectra for the two targets in Fig. 3). The fission spectra observed for other targets, with the exception of  ${}^{208}\text{Pb}$ , are quite similar to those shown for the thicker  ${}^{197}\text{Au}$  target. In the case of  ${}^{208}\text{Pb}$  ( $4.9 \text{ mg/cm}^2$ ), the thick target introduced a severe distortion of the spectrum shape, which prohibited a clear distinction at forward angles between fission fragments and other reaction products stopped in the front counter. We were still able to deduce reliable total fission cross sections for  ${}^{208}\text{Pb}$  from yields measured in the range  $50^\circ \leq \theta_{\text{lab}} \leq 170^\circ$ ; over this range, corresponding to a considerable variation in the mean laboratory kinetic energy of the fission fragments, the observed angular distribution shapes are consistent with those for other targets (see below).

Representative fission-fragment angular distributions are shown in Fig. 4. Complete angular distributions spanning the range  $10^\circ \leq \theta_{\text{lab}} \leq 170^\circ$  were ob-

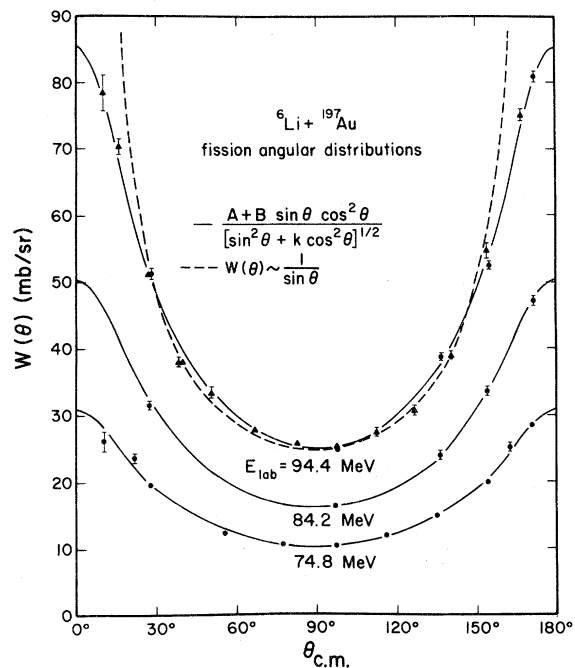


FIG. 4. Representative c.m. angular distributions for the fission fragments. The circles denote measurements made with the  $2.15 \text{ mg/cm}^2$   ${}^{197}\text{Au}$  target and the triangles measurements with the  $0.8 \text{ mg/cm}^2$  target. The kinematic conversion from laboratory to c.m. frame was carried out for equal mass fragments with total kinetic energy equal to the mean value given by the systematics compiled in Ref. 33. The solid curves represent the empirical formula displayed with the parameters  $A$ ,  $B$ , and  $k$  adjusted for optimum fits to the data. Also shown for comparison at  $94.4 \text{ MeV}$  is  $W(\theta) \propto (\sin \theta)^{-1}$ .

tained at at least one bombarding energy for each target other than  ${}^{208}\text{Pb}$ . In all cases the c.m. differential cross sections exhibit a clear symmetry about  $\theta_{\text{c.m.}} = 90^\circ$  (see Fig. 4), as expected for the decay of an equilibrated compound nucleus. There are several effects which might have introduced some asymmetry in the angular distributions: (1) fission from the composite system prior to attainment of thermal equilibrium; (2) fission following the transfer (incomplete fusion<sup>17</sup>) of an  $\alpha$  particle with the beam velocity<sup>34,35</sup> (which would yield  $\sim 20\%$  fore-aft asymmetry when the laboratory cross sections are converted to the c.m. frame via kinematics appropriate to  ${}^6\text{Li}$ -induced fusion-fission); (3) multiple Coulomb scattering of the fragments in the target and neutron emission from the fragments, both of which would yield greater "smearing" of the angular distribution at backward angles than at forward angles, because of the reduced laboratory kinetic energy of the fragments. While it is conceivable that some of these effects might tend to cancel, it seems most likely that all are negligible in light of the persistent observed symmetry of the angular distributions. (The consistency of measurements with the thin and thick  ${}^{197}\text{Au}$  targets also rules out appreciable multiple scattering effects.) In particular, the experimental limits on the fore-aft asymmetry suggest that no more than 10% of the total fission cross section for any of these systems can result from incomplete rather than complete fusion. An even more stringent limit on possible transfer contributions is imposed by the particle-particle coincidence measurements described in Sec. II E. This result is not surprising, even though the  $\alpha$ -transfer cross section is large<sup>34</sup>: The composite system has lower  $Z$ , lower angular momentum, and lower excitation energy than that formed in the  ${}^6\text{Li}$ -induced fusion, and these effects act in concert to severely reduce the fission probability (see Sec. IV C).

Two types of curves are compared with the measured angular distributions in Fig. 4. The dashed curve shown for  $E_{\text{lab}} = 94.4$  MeV varies with c.m. angle as  $1/\sin\theta$ , as would be expected for high-spin fission in the limit in which the angular momentum is completely aligned perpendicular to the symmetry axis of the fissioning nucleus and to the incident beam direction.<sup>20</sup> The significant deviations of the observed distributions from  $1/\sin\theta$  play an important role in the statistical model analysis of the results which is described in Secs. IV and V (see also Refs. 21 and 23). In order to quantify these deviations we have fitted each angular distribution (measurements were always made at at least four angles)

with an empirically constructed formula,

$$W_{\text{fiss}}(\theta) = \frac{A + B \sin\theta \cos^2\theta}{[\sin^2\theta + k \cos^2\theta]^{1/2}} \quad (2)$$

by varying the parameters  $A$ ,  $B$ , and  $k$  to minimize  $\chi^2$ . The solid curves in Fig. 4 represent such fits. Formula (2) is manifestly symmetric about  $\theta = 90^\circ$ , reduces to  $1/\sin\theta$  in the vicinity of  $90^\circ$ , and provides good fits not only to the measurements, but also to the angular distributions calculated in the statistical model treatment described in the following paper. The empirical fits with Eq. (2) are used to extract from the measurements the total fission cross section  $\sigma_{\text{fiss}}$  and the fission-fragment anisotropy

$$\gamma_{\text{fiss}} \equiv W_{\text{fiss}}(\theta_{\text{c.m.}} = 170^\circ) / W_{\text{fiss}}(\theta_{\text{c.m.}} = 90^\circ) \quad (3)$$

### C. Charged-particle emission characteristics

Representative forward- and backward-angle energy spectra for  $Z=1$  and  $Z=2$  products are shown in Fig. 5. At large angles one observes low-energy peaks qualitatively consistent with expectations for evaporation processes. At more forward angles these peaks become buried under large yields of products attributable to breakup, transfer, and preequilibrium mechanisms. This change in the nature of the spectrum is reflected in Fig. 6 in the strong forward peaking exhibited by the inclusive charged-particle angular distributions. ( ${}^3\text{He}$  data have been omitted from Fig. 6 since the backward-angle yield is insignificant.) The observed angular distributions are very similar for all targets and energies studied.

For the present purposes we are interested in the total cross sections for particle emission only from equilibrated compound nuclei. We have extracted these cross sections under the assumption that the evaporation yields are isotropic in the CN rest frame,<sup>36</sup> and are dominant over contributions from other processes at the far backward angles, where the observed angular distributions do indeed flatten out. We have thus taken

$$\sigma_{\text{evap}} = 4\pi \left\langle \frac{d\sigma}{d\Omega_{\text{c.m.}}} \right\rangle_{\text{backward}} \quad (4)$$

with the differential cross section averaged over the range  $130^\circ \leq \theta_{\text{lab}} \leq 170^\circ$  for  $p$  and  $\alpha$ , and over  $150^\circ \leq \theta_{\text{lab}} \leq 170^\circ$  for  $d$  and  $t$ . Some quantitative assessment of the applicability of this assumption can

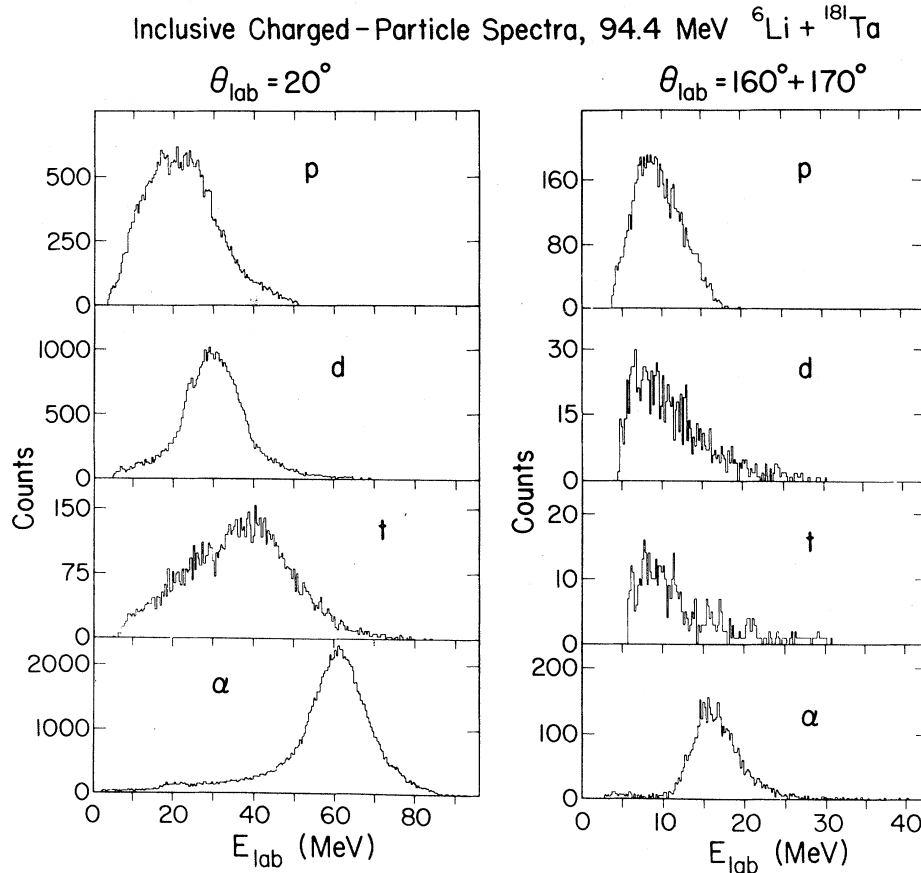


FIG. 5. Representative forward- and backward-angle energy spectra for  $p$ ,  $d$ ,  $t$ , and  $\alpha$  particles. The spectra acquired at  $160^\circ$  and  $170^\circ$  have been summed to improve statistics. The slight discontinuities observed in the forward-angle  $p$ ,  $d$ , and  $t$  spectra, at outgoing particle energies of 19, 25, and 31 MeV, respectively, result from a thin dead layer at the entrance to the fourth (5 mm thick silicon) detector in the telescope. The presence of the dead layer has no effect on the energy-integrated particle yields extracted from the spectra.

be made later (see Sec. V A) by comparing the observed back-angle energy spectra with evaporation predictions. Possible corrections to the evaporation cross sections to account for multiple charged-particle emission or for evaporation following direct reactions will be discussed in Sec. II E. Since the statistical model code we have used does not allow for  $d$  and  $t$  evaporation, we will later compare predicted proton evaporation cross sections with the sum ( $\sigma_{Z=1}$ ) of the measured  $p$ ,  $d$ , and  $t$  cross sections.

#### D. Measurement of $\sigma_{xn}$

The dominant decay mode of the highly excited nuclei studied here is multiple neutron emission, i.e.,  $({}^6\text{Li}, xn)$  reactions. The total cross section ( $\sigma_{xn}$ )

for such reactions cannot be readily determined in analogous fashion to  $\sigma_{Z=1}$  and  $\sigma_\alpha$ —i.e., by measuring the neutron yield itself—since one would have to (a) discriminate against the many neutrons which accompany charged-particle emission or fission, and (b) independently determine the multiplicity of neutrons emitted in the average  $({}^6\text{Li}, xn)$  reaction. It is far more direct to measure the total production cross sections for the  $({}^6\text{Li}, xn)$  residues. However, standard techniques for measuring such “evaporation-residue” cross sections are of limited usefulness in the present case, where the residues have high  $Z$  ( $\sim 80$ ), very low laboratory kinetic energy ( $\sim$  a few MeV), and relatively high level densities and poorly known  $\gamma$ -decay schemes.

In the present experiment we have identified pro-



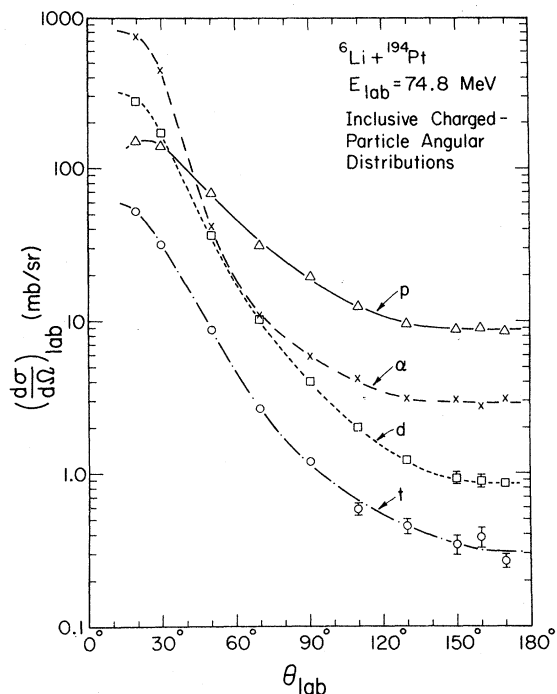


FIG. 6. Measured angular distributions for inclusive production of light charged particles. The curves are only to guide the eye. Total cross sections for evaporation are deduced from the backward-angle differential cross sections, assuming isotropic emission in the c.m. frame.

duction of residues with the same atomic number ( $Z_{\text{CN}}$ ) as the CN via detection of the characteristic prompt  $K$  x rays, which result from  $K$ -shell internal conversion during the  $\gamma$  cascades deexciting the residues.<sup>28,37</sup> Repeated  $K$ -shell conversion (hence, multiple  $K$  x-ray emission) is possible during a single  $\gamma$  cascade because  $K$ -vacancy lifetimes for heavy atoms<sup>38</sup> ( $\sim 10^{-17}$  s) are much shorter than typical nuclear transition lifetimes. The (isotropic) singles yield ( $N_1$ ) of  $Z_{\text{CN}}$   $K$  x rays in a detector of efficiency  $\eta_1$  can be written:

$$N_1 \propto \sigma_{xn} \langle M_K \rangle \eta_1, \quad (5)$$

where  $\sigma_{xn}$  is understood to be summed over all values of  $x$ , and the  $K$  x-ray multiplicity  $\langle M_K \rangle$  is averaged over all  $\gamma$ -decay paths in all ( ${}^6\text{Li}, xn$ ) products. If  $\langle M_K \rangle \gtrsim 1$ , as we observe for all cases studied here, then the multiplicity can be reliably deduced<sup>28</sup> from x-ray-x-ray coincidence yields ( $N_{12}$ ):

$$D \equiv N_{12}/N_1\eta_2 = \langle M_K \rangle \pm 0.2, \quad (6)$$

where  $\eta_2$  is the efficiency of the second x-ray detector. The doubles-to-singles ratio  $D$  would be precisely equal to  $\langle M_K \rangle$  if the frequency distribution of  $M_K$  values were a Poisson distribution. The uncertainty estimate  $\pm 0.2$  included in Eq. (6) is based on detailed statistical considerations<sup>28</sup> of possible systematic deviations from a Poisson multiplicity distribution. The validity of Eq. (6) has been experimentally confirmed in selected cases by measurements of x-ray- $\gamma$ -ray coincidences.<sup>28</sup>

We have determined  $\sigma_{xn}$  experimentally from Eqs. (5) and (6) by measuring the singles and coincidence  $K$  x-ray yields with two or three intrinsic Ge detectors, whose efficiencies were calibrated with radioactive sources. The absolute x-ray production cross sections, and hence  $\sigma_{xn}$ , have been normalized in a manner exactly analogous to our normalization procedure for  $\sigma_{Z=1}$ ,  $\sigma_\alpha$ , and  $\sigma_{\text{fiss}}$ , i.e., against the nearly Rutherford  ${}^6\text{Li}$  elastic scattering yields<sup>39</sup> at  $\theta_{\text{lab}} = 10.0^\circ$ . Further experimental details of the x-ray measurements, and a discussion of the nuclear structure implications of the  $\langle M_K \rangle$  results, are presented elsewhere.<sup>28</sup>

It should be noted that the x-ray multiplicity method could, in principle, be applied as well to the determination of element-production cross sections for  $Z_{\text{CN}} - 1$  and  $Z_{\text{CN}} - 2$ , although in these cases (in contrast to  $Z_{\text{CN}}$ ) large  $\beta$ -activity contributions to the x-ray yields would have to be subtracted. However, this technique would not allow us to distinguish formation of the residues via ( ${}^6\text{Li}, pxn$ ) or ( ${}^6\text{Li}, \alpha xn$ ) evaporation processes, as opposed to incomplete fusion or transfer mechanisms. For this reason we have chosen to determine  $\sigma_\alpha$  and  $\sigma_{Z=1}$  by direct detection of the evaporated charged particles. This possible confusion between residue production by direct versus fusion mechanisms is not serious for  $\sigma_{xn}$ , since  ${}^5\text{Li}$  transfer is viewed as an unlikely process.

#### E. Possible ambiguities in the total fusion cross section

We have deduced the total cross section for CN formation for each target and bombarding energy by summing the contributions corresponding to the four major decay modes [see Eq. (1)]. In this section we discuss possible ambiguities in the resultant values of  $\sigma_{\text{fus}}$  arising from three aspects of our measurement techniques:

(1) The singles charged-particle detection is subject to double counting of contributions to  $\sigma_{\text{fiss}}$ ,  $\sigma_{Z=1}$ , and  $\sigma_\alpha$ , if the CN decay involves any appre-

cialable multiple charged-particle emission or fission following charged-particle evaporation. In contrast, by identifying the production of ( ${}^6\text{Li}, xn$ ) residues, we avoid multiple counting in multiple neutron emission and we exclude from  $\sigma_{xn}$  processes in which neutrons accompany the emission of one or more charged particles (the latter processes contribute instead to  $\sigma_{\text{fiss}}$ ,  $\sigma_{Z=1}$ , or  $\sigma_{\alpha}$ ).

(2) The decay of highly excited nuclei formed in direct reactions (e.g., involving  $\alpha$  and  $d$  transfer) with large cross sections<sup>34,35</sup> may contribute in principle to the singles measurements of  $\sigma_{\text{fiss}}$ ,  $\sigma_{Z=1}$ , and  $\sigma_{\alpha}$ . We have already seen (Fig. 4) some evidence against sizable contributions of this sort in the observed symmetry of the fission-fragment angular distributions, but no comparable evidence is available from the singles evaporation yields.

(3) Our technique for determining  $\sigma_{xn}$  does not discriminate against residues reached via emission from the composite system of one or more preequilibrium neutrons. However, we have specifically tried to avoid including preequilibrium charged-particle emission in  $\sigma_{\text{fus}}$ , by concentrating on the  $Z=1$  and  $\alpha$ -particle yields at far backward angles.

In order to determine the magnitude of effects (1) and (2) above, we have made particle-particle coincidence measurements for a few angle pairs in 95 MeV  ${}^6\text{Li}$  bombardment of  ${}^{194}\text{Pt}$ . We used two silicon-detector telescopes, each capable of identifying  $Z=1$  and  $Z=2$  particles and fission fragments over the full expected energy ranges, one at forward angles ( $\theta_{\text{lab}}=15^\circ$  and  $25^\circ$ ,  $\sim 1$  msr solid angle) and one at backward angles ( $\theta_{\text{lab}}=150^\circ$  and  $165^\circ$ ,  $\sim 4$  msr). Total coincidence cross sections were estimated from the measured yields under the following assumptions: (1) energetic forward-going  $Z=1$  and  $Z=2$  particles detected in coincidence with back-angle products are characterized by laboratory angular distributions similar to the observed *inclusive* distributions for the corresponding particle type and energy; (2) the mass, direction, and energy of the unobserved recoil nucleus corresponding to a detected  $Z=1$  or  $Z=2$  particle are calculated as for a two-body final state; (3) evaporation particles are emitted isotropically in the rest frame of the recoiling residual nucleus (or in the rest frame of the CN when in coincidence with a fission fragment or another evaporation particle); (4) fission fragments are emitted with angular distributions in the recoil-nucleus rest frame similar to those observed in Fig. 4, with an anisotropy  $\gamma_{\text{fiss}}=3.0$ .

Under these assumptions, the particle-particle coincidence measurements reveal that there is no significant double counting introduced when we

sum  $\sigma_{\text{fiss}}$ ,  $\sigma_{Z=1}$ , and  $\sigma_{\alpha}$ . We are able to place meaningful upper limits on multiple charged-particle evaporation ( $< 5\%$  of the corresponding singles yields) and on fission following charged-particle evaporation or direct reactions ( $< 3\%$  of  $\sigma_{\text{fiss}}$ ). [The small probabilities for these processes reflect largely the Coulomb barrier hindrance and the large excitation-energy removal associated with charged-particle emission from heavy nuclei; the experimental limits are completely consistent with statistical model expectations (see Sec. IV C).] At the same time, we find that for  ${}^{194}\text{Pt}$  at 95 MeV,  $(13 \pm 2)\%$  of  $\sigma_{Z=1}$  and  $(8 \pm 2)\%$  of  $\sigma_{\alpha}$  deduced from Eq. (4) are associated with evaporation following direct, preequilibrium, or incomplete fusion reactions giving rise to energetic charged products. The raw cross sections from the singles measurements have been correspondingly reduced. Since the forward-angle energetic charged-particle production cross sections are quite similar for all targets and energies studied, we assumed it reasonable to reduce the charged-particle evaporation cross sections by similar factors [ $(0.87 \pm 0.06)$  for  $\sigma_{Z=1}$  and  $(0.92 \pm 0.04)$  for  $\sigma_{\alpha}$ ] for all cases. The indicated uncertainties in these reduction factors are included in the errors assigned to the corrected experimental values for  $\sigma_{Z=1}$  and  $\sigma_{\alpha}$ .

The asymmetry in our experimental treatment of charged-particle versus neutron *preequilibrium* emission is, to first order, appropriate for our purposes. For our later analysis we want  $\sigma_{\text{fus}}$  to include all those processes which may lead with appreciable probability to subsequent fission or charged-particle evaporation. Our particle-particle coincidence measurements and our statistical model calculations together demonstrate that fission and charged-particle evaporation are far less likely following emission of an energetic  $p$  or  $\alpha$  than following emission of an energetic neutron. (In any case, contributions of the former sort have already been subtracted in the correction procedure described above for  $\sigma_{Z=1}$  and  $\sigma_{\alpha}$ .) If we do indeed find evidence in our measurements for significant preequilibrium particle emission, then we should be prepared to incorporate somehow in our statistical model calculations the associated changes (relative to pure equilibrium decay) in the excitation energy and angular momentum distributions of nuclei along the decay chain which undergo fission and charged-particle evaporation.

### III. EXPERIMENTAL RESULTS

The measured absolute total cross sections ( $\sigma_{Z=1}$ ,  $\sigma_{\alpha}$ ,  $\sigma_{\text{fiss}}$ ,  $\sigma_{xn}$ , and  $\sigma_{\text{fus}}$ ), fission-fragment an-

TABLE I. Experimental results for  ${}^6\text{Li}$ -induced fusion decay.

Target	$E_{\text{lab}}$ (MeV)	$\sigma_{Z=1}^a$ (mb)	$\sigma_{\alpha}^a$ (mb)	$\sigma_{\text{fiss}}^b$ (mb)	$\gamma_{\text{fiss}}^c$	$\langle M_K \rangle^d$	$\sigma_{xn}^e$ (mb)	$\sigma_{\text{fus}}^f$ (mb)
${}^{181}\text{Ta}$	74.8	$136 \pm 12.3$	$56.5 \pm 3.4$	$2.1 \pm 0.1$	$3.20 \pm 0.52$	$1.16 \pm 0.26$	$1127 \pm 265$	$1322 \pm 274(355)$
	84.2	$163 \pm 14.7$	$75.3 \pm 4.6$	$4.6 \pm 0.2$	$2.73 \pm 0.20$	$1.25 \pm 0.21$	$1023 \pm 208$	$1266 \pm 220(303)$
	94.4	$206 \pm 18.5$	$103.0 \pm 6.0$	$8.8 \pm 0.3$	$3.19 \pm 0.14$	$1.03 \pm 0.25$	$1329 \pm 360$	$1647 \pm 371(460)$
${}^{198}\text{Pt}$	74.8	$93 \pm 8.5$	$21.5 \pm 1.4$	$15.9 \pm 0.5$	$2.62 \pm 0.11$	$3.05 \pm 0.34$	$1110 \pm 127$	$1241 \pm 142(216)$
	84.2	$105 \pm 9.8$	$30.3 \pm 2.2$	$28.2 \pm 1.1$	$2.63 \pm 0.12$	$3.21 \pm 0.16$	$1034 \pm 99$	$1198 \pm 118(194)$
	94.4	$123 \pm 11.1$	$44.4 \pm 2.7$	$47.6 \pm 1.3$	$3.18 \pm 0.09$	$3.21 \pm 0.22$	$1049 \pm 75$	$1264 \pm 101(188)$
${}^{194}\text{Pt}$	74.8	$112 \pm 10.2$	$37.9 \pm 2.4$	$50.8 \pm 1.5$	$2.87 \pm 0.07$	$3.00 \pm 0.40^g$	$987 \pm 135$	$1188 \pm 148(209)$
	84.2	$139 \pm 12.8$	$56.4 \pm 3.7$	$87.2 \pm 2.6$	$2.79 \pm 0.10$	$3.12 \pm 0.17$	$904 \pm 94$	$1187 \pm 115(181)$
	94.4	$177 \pm 16.0$	$78.7 \pm 4.8$	$136 \pm 3.9$	$3.06 \pm 0.08$	$3.15 \pm 0.35$	$775 \pm 89$	$1167 \pm 112(169)$
${}^{197}\text{Au}$	74.8	$107 \pm 9.8$	$34.2 \pm 2.6$	$87.6 \pm 2.5$	$2.71 \pm 0.05$	$2.15 \pm 0.26$	$653 \pm 81$	$882 \pm 94(138)$
	84.2	$128 \pm 11.9$	$50.5 \pm 3.9$	$139 \pm 4.1$	$2.84 \pm 0.08$	$2.25 \pm 0.13$	$578 \pm 52$	$896 \pm 76(123)$
	94.4	$150 \pm 13.7$	$72.1 \pm 5.4$	$220 \pm 6.2$	$3.15 \pm 0.04$	$1.83 \pm 0.29$	$732 \pm 128$	$1174 \pm 147(193)$
${}^{208}\text{Pb}$	74.8	$124 \pm 11.2$	$17.0 \pm 1.1$	$160 \pm 6.4$	$3.12 \pm 0.29$	$1.70 \pm 0.13$	$1055 \pm 94$	$1356 \pm 117(199)$
	84.2	$121 \pm 11.1$	$24.7 \pm 1.7$	$224 \pm 9.0$	$3.22 \pm 0.11$	$2.24 \pm 0.17$	$719 \pm 67$	$1089 \pm 93(152)$
	94.4	$135 \pm 12.2$	$34.2 \pm 2.1$	$342 \pm 13.4$	$2.80 \pm 0.09$	$2.34 \pm 0.21$	$807 \pm 77$	$1318 \pm 111(177)$

<sup>a</sup>The charged-particle evaporation cross sections have been corrected to subtract contributions following direct reactions, as explained in the text. The quoted errors include, in addition to counting statistics, the estimated uncertainties in these correction factors and *relative* errors (which may differ from one target and energy to the next) arising from the normalization procedure and isotropy assumption.

<sup>b</sup>The errors in  $\sigma_{\text{fiss}}$  include statistical uncertainties in fitting Eq. (2) to the measured differential cross sections and relative normalization uncertainties.

<sup>c</sup>The errors in  $\gamma_{\text{fiss}}$  are primarily statistical [from fitting with Eq. (2)], but allow for small possible systematic deviations of the actual angular distributions from the assumed form.

<sup>d</sup>The errors in  $\langle M_K \rangle$  arise mainly from background subtraction uncertainties in the x-ray singles and coincidence spectra and from coincidence counting statistics. They do not include the  $\pm 0.2$  systematic uncertainty from Eq. (6).

<sup>e</sup>The errors in  $\sigma_{xn}$  arise from the same sources as for  $\langle M_K \rangle$ , plus relative normalization uncertainties for the x-ray cross sections.

<sup>f</sup>In addition to the indicated relative errors in the component cross sections, the errors in  $\sigma_{\text{fus}}$  include estimated overall absolute normalization uncertainties  $\sim \pm 5\%$  in both  $\sigma_{xn}$  and the charged-particle cross sections. The numbers in parentheses represent  $\sigma_{\text{fus}}$  errors including also  $\pm 10$ – $15\%$  systematic errors in  $\sigma_{xn}$  associated with possible deviations from Poisson x-ray multiplicity distributions [see Eq. (6)].

<sup>g</sup>This  $\langle M_K \rangle$  value was not measured, but has been assumed on the basis of observed systematics.

isotropies ( $\gamma_{\text{fiss}}$ ), and  ${}^6\text{Li}, xn$   $K$  x-ray multiplicities ( $\langle M_K \rangle$ ) are specified in Table I, along with a summary of the sources of the quoted uncertainties. A graphic presentation of the division of  $\sigma_{\text{fus}}$  among the four major decay modes is given in Fig. 7 for the five targets studied at two bombarding energies. It can be seen that  $\sigma_{xn}$  is the dominant contribution to  $\sigma_{\text{fus}}$  in all the cases studied. The charged-particle evaporation cross sections exhibit a mild dependence on both target and bombarding energy; a significantly stronger sensitivity to both is seen for  $\sigma_{\text{fiss}}$ . The targets have been arranged from left to right in order of increasing values of  $Z^2/A$  (i.e., increasing fissility) for the CN, and the corresponding

increase observed for  $\sigma_{\text{fiss}}$  is qualitatively consistent with liquid-drop expectations. In contrast, as may be seen from Table I,  $\gamma_{\text{fiss}}$  is at most weakly dependent on target and bombarding energy. A quantitative analysis of these dependences will be presented in Sec. V.

The solid  $\sigma_{\text{fus}}$  error bars in Fig. 7 represent the overall absolute cross section measurement uncertainties (see Table I). These are dominated by uncertainties in  $\sigma_{xn}$ , which in turn arise from counting statistics in the x-ray–x-ray coincidence yields, from background subtraction in the x-ray spectra, and from uncertainties ( $\sim \pm 5\%$ ) in the absolute normalization procedure. The dashed error bars in

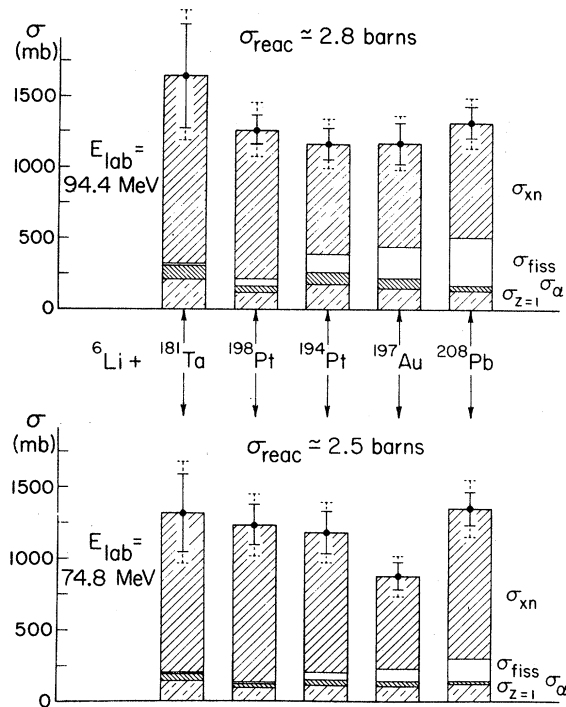


FIG. 7. Decomposition of the measured fusion cross section for five targets at two energies. The solid and dashed error bars are explained in the text. Total reaction cross sections from optical model calculations are indicated for each energy.

Fig. 7 (corresponding to the errors in parentheses in Table I) include an estimate of the additional systematic uncertainty [see Eq. (6)] associated with possible deviations of the x-ray multiplicity distributions from the assumed Poisson form. Within the errors there is no real evidence for any significant dependence of  $\sigma_{\text{fus}}$  on target or bombarding energy. The largest observed anomalies in the  $\sigma_{\text{fus}}$  results (see Table I) are the low values for  ${}^6\text{Li} + {}^{197}\text{Au}$  at 74.8 and 84.2 MeV; while we have no reason for expecting any greater systematic error in these cases than in all others, we are nonetheless not confident that the anomaly is real. Since the statistical model predictions are very sensitive to the value one inputs for  $\sigma_{\text{fus}}$ , and since the largest fluctuations in measured  $\sigma_{\text{fus}}$  values are of marginal significance, we will later compare measurements to two types of calculations: one which uses the individual measured  $\sigma_{\text{fus}}$  values, with (the dashed) error bars, and a second employing for all cases the value  $\langle\sigma_{\text{fus}}\rangle = 1213$  mb, obtained by averaging over the measurements for all targets and bombarding energies.

It should be noted that  $\langle\sigma_{\text{fus}}\rangle$  corresponds to roughly *half* of the total reaction cross sections ( $\sigma_{\text{reac}}$ ) expected for these systems from optical model calculations. The ratio  $\sigma_{\text{fus}}/\sigma_{\text{reac}} \sim 0.5$  is similar to that observed with heavier projectiles on much lighter target nuclei at comparable energies per nucleon (e.g., see Ref. 16). In the present cases, most of the remainder of  $\sigma_{\text{reac}}$  is exhausted by various types of projectile fragmentation (simple “elastic” breakup, incomplete fusion, etc.).

#### IV. STATISTICAL MODEL ANALYSIS

##### A. General features of the calculations

A statistical model analysis of the decay of the compound systems investigated has been carried out with the code MBEGAT, the underlying assumptions and computational details of which are explained in the following paper.<sup>23</sup> The relative decay widths for fission and for neutron, proton, and  $\alpha$ -particle evaporation are evaluated as functions of angular momentum and excitation energy in each emitting nuclide along the CN decay chain. The calculation of fission widths is based on the Bohr-Wheeler transition-state formalism<sup>40</sup> and the evaporation widths on a Hauser-Feshbach approach, which includes proper angular momentum coupling at each stage of the decay.

MBEGAT is an extensively modified version of the Beckerman-Blann code MB-II (Ref. 30). Two of the major modifications we have made—incorporating a calculation of the fission-fragment angular distribution and improving the level density treatment for the deformed nuclei relevant to both fission and particle emission—are discussed in detail in the following paper.<sup>23</sup> A third modification, allowing for simulation of the effects of preequilibrium particle emission on the subsequent equilibrium decay, is described, together with its influence on our analysis, in Sec. V B of the present paper. Most of the calculations we present here do not include the latter change, and include our level density improvements only partially. Specifically, we evaluate level densities at the yrast (for particle emission) and saddle-point (for fission) shapes predicted by the RLDM,<sup>1</sup> using in both cases a deformed-nucleus Fermi-gas treatment<sup>22</sup> which *fully includes* the collective rotational bands built upon each intrinsic configuration [see Eqs. (33) and (34) in the following paper]. While this approach represents a significant improvement in principle over the usual (Refs. 5–7, 11, 12, and 23) spherical-nucleus treat-

ment of the level densities, it neglects the dilution of the collective level density enhancement which must set in with increasing excitation,<sup>22</sup> at different rates for the yrast and saddle-point deformations. In the following paper<sup>23</sup> we propose a somewhat speculative method for taking account of this dilution, and in Sec. VC of the present paper we explore its consequences for our comparison of measurements and calculations. A number of additional effects omitted in the present (and many previous) statistical model calculations, but expected to cause only minor changes in our results, are specified in Sec. IV D.

It should be kept in mind that the output of any statistical model calculation depends very strongly on a wide variety of parameters describing aspects of the nuclear structure and of the mechanisms for CN formation and particle emission. The most important parameters, and our justification for adopting the specific values used in the present calculations, are discussed in the following subsection. In Sec. IV C we investigate the quantitative sensitivity of the calculations to variations in some of these parameters.

### B. Choice of parameters

In Sec. V A we compare our measurements to the results of statistical model calculations employing *no adjustable parameters*. It is important to specify our choice of parameter values in some detail, since the choice involves several significant subtle or controversial points.

Our approach is to fix *all* of the relevant nuclear structure information according to the predictions of the RLD and NIFG models. Consistency requires that if we neglect shell and pairing corrections, we do so *completely*, as should be appropriate in the high-temperature limit.<sup>25,27</sup> Thus, for example, the ground-state masses of all nuclides in the decay chain, and hence the  $n$ ,  $p$ , and  $\alpha$  binding energies, are determined from the liquid-drop model. It is also important for consistency to use the LDM mass for the CN (but experimental masses for the projectile and target nuclei, which are cold) in computing the initial excitation energy  $E_{\text{CN}}^*$ ; we thus use a “hybrid” effective  $Q$  value for the fusion reaction:

$$Q_{\text{eff}} = c^2 [m_{\text{proj}}^{\text{expt}} + m_{\text{targ}}^{\text{expt}} - m_{\text{CN}}^{\text{LDM}}] . \quad (7)$$

The yrast energies and moments of inertia (needed for evaluation of the particle-emission level densities  $\rho_v$ ) and the saddle-point energies and moments of inertia [needed in calculating the fission level

densities  $\rho_f$  and the angular distribution  $W_{\text{fiss}}(\theta)$ ] are taken from the RLDM predictions of Cohen, Plasil, and Swiatecki.<sup>1</sup> It should be noted that the  $N$ ,  $Z$ , and  $J$  dependences of these structure properties are all completely determined by the RLDM, and would probably have to be independently parametrized in a less constrained (parameter-search) approach to the statistical model calculations.

The Fermi-gas level density parameter  $a$ , which determines the rate of increase of  $\rho$  with  $E^*$ , is directly related to the single-particle level density ( $g_0$ ) at the Fermi energy, and should be proportional to mass number  $A$  (e.g., see Ref. 27). The proportionality constants are chosen in the present work to be the same for  $n$ ,  $p$ , and  $\alpha$  emission, each of which leaves the residual nucleus at relatively small (yrast) deformation:

$$a_n = a_p = a_\alpha = A/9.0 , \quad (8)$$

where  $A$  is the mass number of the *final* nucleus. The proportionality constant here is based on calculations<sup>26,41</sup> of *smoothed* shell-model single-particle spectra in the Pb region.

The level density parameter relevant to fission is given by an expression of the same form as Eq. (8), but with  $A$  representing the mass number of the *fissioning* nucleus and a proportionality constant differing from 1/9.0 by a factor denoted by the parameter  $a_f/a_n$ . One would expect  $g_0$  to be shape independent, and hence  $a_f/a_n$  to be unity, for a NIFG with *uniform particle density* (for which  $g_0 \propto A^{1/3} V^{2/3}$ , where  $V$  is the volume of the container). In a realistic model of a nucleus, however, one must take account of the *diffuse surface* region, where the matter density is lower than the central value. Since the surface-to-volume ratio increases with increasing nuclear deformation, a corresponding small increase in the volume, and hence in  $g_0$ , is necessary to conserve the total number of nucleons. This deformation dependence has been estimated quantitatively by Bishop *et al.*,<sup>42</sup> who deduce a simple functional dependence of  $g_0$  on the major-to-minor axis ratio  $r$  of the nucleus.

We have based our choice of  $a_f/a_n$  values on Bishop’s calculations<sup>42</sup> and on RLDM predictions<sup>1</sup> for the saddle-point axis ratio  $r_{\text{sad}}$  in a typical fissioning nucleus (halfway down the evaporation chain) with spin  $J \approx 25\hbar$ . (At the yrast deformation in our cases,  $r$  does not deviate sufficiently from unity to yield any appreciable change in  $g_0$  from that for a spherical nucleus.) In our mass region  $r_{\text{sad}}$  varies quite slowly with spin, but rapidly with  $Z^2/A$ , e.g., from 4.9 for  ${}^{184}\text{Os}$  (the “typical” fission-

ing nucleus for  ${}^6\text{Li} + {}^{181}\text{Ta}$ ) to 2.8 for  ${}^{210}\text{At}$  ( ${}^6\text{Li} + {}^{208}\text{Pb}$ ). There is correspondingly a variation in  $a_f/a_n$  with target nucleus: We use  $a_f/a_n = 1.067, 1.046, 1.043, 1.039,$  and  $1.029$  for  ${}^{181}\text{Ta}, {}^{198}\text{Pt}, {}^{194}\text{Pt}, {}^{197}\text{Au},$  and  ${}^{208}\text{Pb},$  respectively. The calculated  $\sigma_{\text{fiss}}$  is extremely sensitive to  $a_f/a_n$  (see Sec. IV C) so that this 4% variation over our range of target nuclei is quite significant.

Aside from these nuclear structure parameters, we need to specify the initial CN spin distribution  $\sigma_{\text{CN}}(J),$  and a prescription for calculating the particle-emission barrier transmission coefficients  $T_\nu^l(\epsilon)$  as a function of particle type ( $\nu$ ), orbital angular momentum ( $l$ ), and kinetic energy ( $\epsilon$ ). In most previous statistical model calculations, the spin distribution has been assumed to have a sharp cutoff at some well-defined value of  $J.$  We make the more realistic assumption of a diffuse (Fermi-function) falloff:

$$\sigma_{\text{CN}}(J) = \pi \lambda^2 \frac{(2J+1)}{1 + \exp[(J - J_0)/d_J]} \quad (9)$$

where  $\lambda$  is the entrance-channel de Broglie wavelength. Although we have performed some calculations investigating sensitivity to the spin-diffuseness

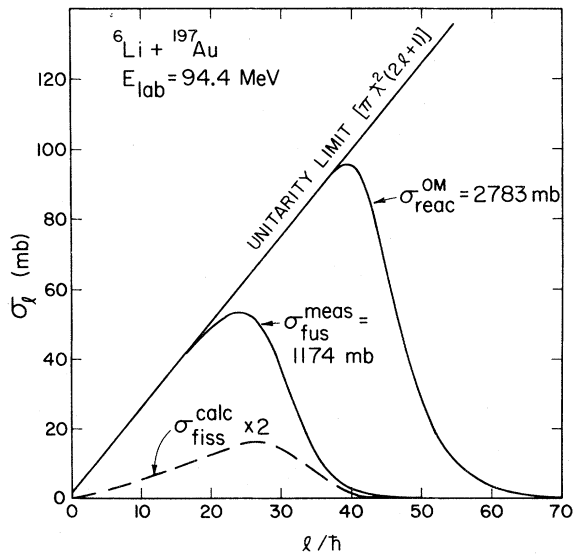


FIG. 8. The angular momentum distributions relevant to the total cross sections for all reactions, for fusion, and for fission. For  $\sigma_{\text{reac}}$ , the magnitude and shape of the curve are given by optical model calculations; for  $\sigma_{\text{fus}}$ , the shape is assumed and the area underneath the curve fixed by measurement; for  $\sigma_{\text{fiss}}$ , the magnitude and shape result from statistical model calculations described in the text.

parameter  $d_J,$  in most of our calculations we have fixed it to the value characteristic of the partial-wave distribution for the *total reaction* cross section, given by optical model (OM) calculations for our  ${}^6\text{Li}$ -target systems. Using a fixed  ${}^6\text{Li}$  potential (determined from an analysis<sup>31</sup> of 99-MeV elastic scattering from  ${}^{208}\text{Pb}$ ), these OM calculations suggest a negligible dependence of  $d_J$  on target, but an appreciable dependence on bombarding energy:  $d_J = 2.55$  at 74.8 MeV, 2.72 at 84.2 MeV, and 2.90 at 94.4 MeV. Once  $d_J$  is chosen, the parameter  $J_0$  in Eq. (9) is constrained to ensure that

$$\sum_J \sigma_{\text{CN}}(J) = \sigma_{\text{fus}}^{\text{measured}}. \quad (10)$$

The angular momentum distributions of  $\sigma_{\text{reac}}$  (from an OM calculation) and of  $\sigma_{\text{fus}}$  [from Eqs. (9) and (10)] are compared for one case in Fig. 8. While our assumption of similar shapes for the two curves seems reasonable, we have neither sufficient experimental information on the fusion distribution nor sufficient theoretical understanding of the fusion mechanism to justify it in any detail.

The difference between fusion and total reaction cross sections for *light* projectiles bears on the choice of prescription for the  $T_\nu^l(\epsilon)$ . Ideally, one should base penetrabilities for particle emission from hot nuclei on cross sections for the time-reversed reaction, i.e., *fusion* of low-energy  $n, p,$  and  $\alpha$  particles with *hot target nuclei*. The latter processes are unfortunately not subject to laboratory investigation, and so one needs to employ a suitable approximation. McMahan and Alexander<sup>43</sup> have argued for the use of measured fusion cross sections on cold target nuclei, while the more traditional approach has been to use optical model calculations of  $T_\nu^l(\epsilon),$  which are tied to total reaction cross sections for cold target nuclei. Since for low-energy projectiles  $\sigma_{\text{fus}}$  is typically substantially smaller than  $\sigma_{\text{reac}}$  (e.g., see Ref. 43), this choice has considerable influence on statistical model calculations of evaporation energy spectra.

We have opted here for the traditional approach. Fusion of low-energy projectiles with cold nuclei must be substantially inhibited simply by *Pauli-blocking* effects—i.e., the unavailability of nearby single-particle states into which inner-shell nucleons can scatter—and this inhibition must fade with increasing temperature of the target nucleus. On this basis, one should expect the ratio  $\sigma_{\text{fus}}/\sigma_{\text{reac}}$  to be significantly closer to unity for hot target nuclei than for targets in their ground state. At the same time, there should be a slow increase in the effective size of the target nucleus, and hence in  $\sigma_{\text{reac}},$  with

increasing temperature, as more single-nucleon states with high quantum numbers become occupied.<sup>44,45</sup> The net effect should be to make  $\sigma_{\text{fus}}$  for a hot nucleus similar in magnitude to  $\sigma_{\text{reac}}$  for a cold nucleus. The use of OM calculations for  $T_{\nu}^l(\epsilon)$  can thus be justified qualitatively, although not quantitatively. In our calculations we take the  $n$ ,  $p$ , and  $\alpha$  OM parameters from relevant low-energy elastic scattering studies specifically for targets in the Pb region.<sup>46</sup>

The nuclei from which particles are emitted during the decay are not only hot, but in general are deformed as well. Beckerman and Blann<sup>47</sup> have emphasized that large deformations may cause dramatic changes in the transmission coefficients, leading, for example, to enhanced  $\alpha$  decay. We have ignored deformation effects on the  $T_{\nu}^l(\epsilon)$  in most of the present calculations, since particle emission has been assumed to populate nuclei at the RLDM yrast deformation, and in our mass and spin region this deformation is small (e.g., major-to-minor axis ratios are less than 1.10). However, in Sec. VC we consider calculations in which particle emission populates residual nuclei at significantly greater deformation, and there we estimate the effect of this increased deformation on the particle decay widths, using a method outlined in the following paper.<sup>23</sup>

It is clear from the above discussion that some significant uncertainties remain regarding the appropriate input for the statistical model calculations, even within the confines of our restrictive structure assumptions. The validity of some of our educated guesses can be assessed *a posteriori* from the comparison of calculations with our wide range of measured quantities. One should keep in mind that the uncertainties would be greatly multiplied if we attempted to include shell and pairing corrections consistently in *all* aspects of the nuclear structure. This, again, is why we consider it more reasonable to use pure RLDM-NIFG nuclear structure at this stage of the statistical model analysis.

### C. Characteristics of the calculations and sensitivity to input parameters

In order to assess the quality of agreement when we subsequently compare our statistical model calculations with experimental results, it is useful first to examine some characteristics and parameter sensitivities of the calculations.

One important feature of the statistical model results, namely, the spin distribution of the calculated

fission cross section, is indicated in Fig. 8. It is seen there that at 94.4 MeV bombarding energy the maximum contributions to fission come from spins of 25–30 $\hbar$ . This region is somewhat beyond the peak in the assumed CN population distribution, reflecting the increase in fission probability with increasing spin. In contrast, the calculated relative partial widths for  $n$ ,  $p$ , and  $\alpha$  evaporation exhibit relatively little spin sensitivity, a result which differs from the situation for substantially lighter emitting nuclides,<sup>6,47</sup> because in our cases the large moments of inertia yield relatively “flat” yrast lines. Consequently, for an emitted particle of given energy the intrinsic excitation, and hence level density, in the daughter nucleus is not enormously greater when the particle emission reduces the nuclear spin than when it increases it by a like amount. Thus, the reduction in mean nuclear spin accompanying particle emission in our cases is small (typically 0.3 $\hbar$  per neutron).

It is also instructive to consider the “chance” distributions characteristic of fission and charged-

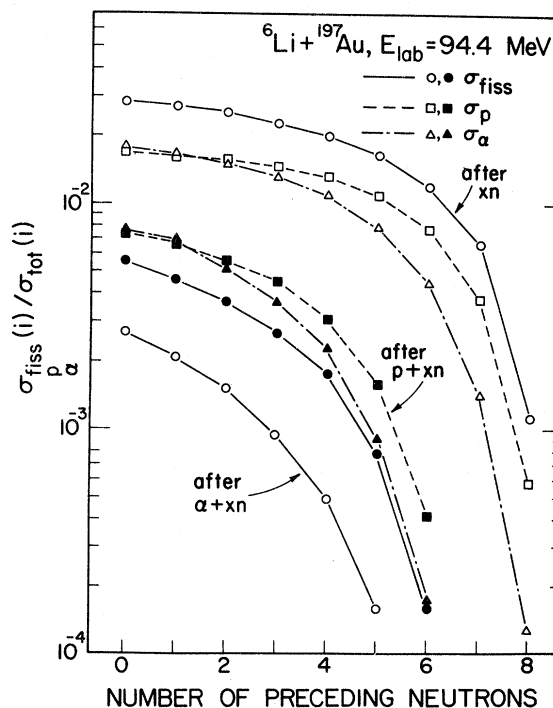


FIG. 9. Calculated chance distributions for fission and charged-particle evaporation probabilities at each stage of the decay of  ${}^{203}\text{Pb}$  formed in 94.4 MeV  ${}^6\text{Li} + {}^{197}\text{Au}$  fusion. The curves for  $\sigma_p$  and  $\sigma_\alpha$  following  $\alpha + xn$  emission are not shown since they are very similar to those following  $p + xn$  emission. The contributions following  $p$  and  $\alpha$  emission account for  $\leq 2\%$  of the total calculated cross sections  $\sigma_{\text{fiss}}$ ,  $\sigma_p$ , and  $\sigma_\alpha$ .

particle evaporation (i.e., the variation of the decay probabilities along the evaporation chain). In Fig. 9, we have plotted the calculated fraction of the total population cross section for a given nuclide in the decay chain which leads to fission,  $p$ , or  $\alpha$  decay, as a function of the number of neutrons emitted from the CN to reach the nuclide in question. Nuclides reached via  $({}^6\text{Li},xn)$ ,  $({}^6\text{Li},pxn)$ , and  $({}^6\text{Li},\alpha xn)$  processes are included in the figure. For any one nuclide the three fractions plotted do not sum to unity; the missing fraction is accounted for by neutron decay or, near the very end of the chain, by  $\gamma$  decay (which is not treated explicitly in the calculations).

The chance distributions displayed in Fig. 9 result from effects associated, on the one hand, with the change in neutron excess, and on the other, with the change in nuclear temperature, accompanying particle emission. Let us concentrate first on the decay of nuclides reached by emission of neutrons only (the top three curves in Fig. 9). Emission of each neutron reduces the neutron excess in the decaying nucleus, leading to an increase in the binding energy  $B_n$  relevant to subsequent neutron emission, but to a decrease in  $B_p$  and  $B_\alpha$ . (Since  $\alpha$  particles are unbound in heavy nuclei—their emission impeded by the Coulomb barrier— $B_\alpha$  actually becomes more negative.) The binding energies change smoothly with neutron number when LDM masses are used. There is a simultaneous reduction in the fission barrier height  $B_{\text{fiss}}$ , since  $Z^2/A$  increases. (The mean spin in the decaying nuclei decreases as more neutrons are emitted, but as mentioned above, this variation is very slow for heavy nuclei, and any consequent effect on  $B_{\text{fiss}}$  is much less important than that from the  $Z^2/A$  increase.) The result of these variations in relative barrier heights is to *enhance* high-chance fission and charged-particle evaporation, at the expense of neutron emission.

In the calculations in Fig. 9, this enhancement is counterbalanced by the temperature dependence of the relative decay widths, since the magnitude of  $B_n$  remains smaller than  $B_{\text{fiss}}$ ,  $B_p + V_p^{\text{Coul}}$ , and  $B_\alpha + V_\alpha^{\text{Coul}}$  (where  $V^{\text{Coul}}$  represents the Coulomb barrier which must be penetrated by an emitted proton or  $\alpha$  particle). A given absolute reduction in overall excitation energy of the decaying nucleus, as accompanies  $n$  emission, thus causes a *larger fractional decrease* in the intrinsic excitation energies and level densities relevant to subsequent fission,  $p$ , and  $\alpha$  decay than in those relevant to subsequent  $n$  decay. It should be kept in mind, however, that the temperature dependence of the decay widths, and hence the chance distributions, might differ strong-

ly from the results in Fig. 9 if the nuclear structure parameters were chosen to deviate significantly from RLDM-NIFG values (see Fig. 11).

Emission of a proton or  $\alpha$  particle tends to reduce the temperature of the decaying nucleus more than neutron evaporation, and furthermore *increases* the relative neutron excess  $[(N-Z)/A]$ , so that the two effects discussed above *reinforce* one another. The net result is a *rapid* decrease in the probability for subsequent charged-particle emission or fission, so that the curves in Fig. 9 representing nuclides reached in  $({}^6\text{Li},pxn)$  and  $({}^6\text{Li},\alpha xn)$  processes are much lower than the curves for  $({}^6\text{Li},xn)$  nuclides. The suppression is particularly strong for *fission* following charged-particle emission since  $B_{\text{fiss}}$  increases rapidly with decreasing  $Z$  of the decaying nucleus.

One may conclude from Fig. 9 that multichance fission and charged-particle evaporation, following emission of a sizable number of neutrons, are important processes to include in the statistical model calculations, while the contributions arising after the emission of a *charged* particle may be safely neglected in the mass region of interest here. In the calculations for 94.4 MeV  ${}^6\text{Li} + {}^{197}\text{Au}$  the latter

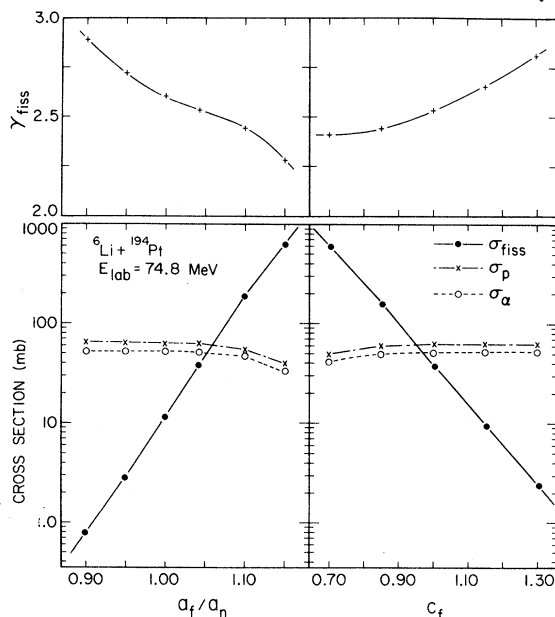


FIG. 10. Variation of the calculated values for the fission cross section and anisotropy, and for the  $p$  and  $\alpha$  evaporation cross sections, with the level density parameter ratio  $a_f/a_n$  and with the fission barrier scaling parameter  $C_f$ . All parameters other than the one varied have the values characteristic of the master parameter set (see Sec. IV B).



contributions account for  $\lesssim 2\%$  of the total cross sections  $\sigma_p$ ,  $\sigma_\alpha$ , and  $\sigma_{\text{fiss}}$ , in good agreement with the results of our particle-particle coincidence measurements discussed in Sec. II E. In the subsequent calculations we present, the contributions associated with the lower four curves in Fig. 9 have indeed been neglected (cutting computing time by more than a factor of 2).

As detailed in the following paper,<sup>23</sup> both the spin and chance distributions for the calculated fission cross section are significantly affected by our use of a deformed-nucleus level density treatment in place of the more usual spherical treatment. Remaining ambiguities in the formalism for including collective level density enhancements give rise to appreciable uncertainties in the fission calculations.<sup>23</sup> While these theoretical uncertainties should not be neglected (they will be further addressed in Sec. V C), it is important to realize that they are small in comparison with the changes in calculational results which would arise from even minor alterations in some of the input parameters. In Fig. 10, for example, we illustrate the sensitivity of the calculations to the level density parameter ratio  $a_f/a_n$  and to the scaling parameter  $C_f$  by which all RLDM fission barrier heights are multiplied.<sup>48</sup> In the calculations represented in Fig. 10 only a single parameter at a time has been varied from the starting values prescribed earlier:  $a_f/a_n$  from its initial value of 1.043 on the left-hand side, and  $C_f$  from 1.00 on the right-hand side. It is obvious that  $\sigma_{\text{fiss}}$  is extremely sensitive to both of these parameters, increasing by three orders of magnitude when  $a_f/a_n$  is increased by  $\sim 25\%$  or when  $C_f$  is reduced by a factor  $\simeq 2$ . Previous analyses of high-spin fission measurements<sup>5-12</sup> have led to claims of necessary parameter adjustments over just such ranges in  $a_f/a_n$  and in  $C_f$ . The changes in  $C_f$  and  $a_f/a_n$  have no direct effect on the partial decay widths  $\Gamma_p$  and  $\Gamma_\alpha$ ; they lead to small changes in  $\sigma_p$  and  $\sigma_\alpha$  when  $\Gamma_{\text{fiss}}$  becomes a sizable fraction of  $\Gamma_{\text{tot}}$ .

We see in Fig. 10 that an increase of  $a_f/a_n$  and a decrease in  $C_f$  have apparently similar effects not only on  $\sigma_{\text{fiss}}$ , but also on  $\gamma_{\text{fiss}}$ . One might be tempted to conclude from this observation that it is generally possible to make simultaneous changes of like sign in  $a_f/a_n$  and in  $C_f$  which leave both  $\sigma_{\text{fiss}}$  and  $\gamma_{\text{fiss}}$  essentially unaltered. However, this conclusion is invalid because the two parameters have strongly correlated effects on the temperature dependence of the relative fission width, and hence on  $\gamma_{\text{fiss}}$ , as illustrated in Fig. 11.

Concentrate first on the calculations labeled A, B, D, and E in Fig. 11. These differ from one another

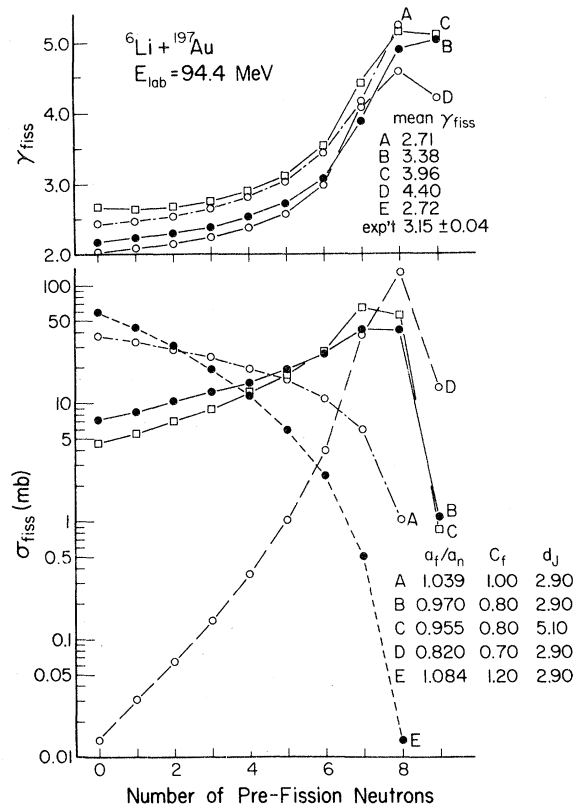


FIG. 11. Calculations illustrating the variation of the fission anisotropy and cross section with chance for five different parameter sets, each reproducing the measured total fusion cross section and yielding the same total fission cross section to within  $\pm 5\%$ . The mean  $\gamma_{\text{fiss}}$  values listed refer to  $W_{\text{fiss}}(\theta)$  summed over all chances. The  $\gamma_{\text{fiss}}$  curve for parameter set E (not shown) falls between those for A and C.

in that  $a_f/a_n$  and  $C_f$  have been changed as appropriate to maintain a constant value for the total fission cross section. (In addition, of course, all the calculations are constrained to match the same measured fusion cross section.) We see in the upper part of Fig. 11 that the calculated anisotropy  $\gamma_{\text{fiss}}$  for any given chance of fission exhibits an appreciable, but not dramatic, sensitivity to these parameter variations; in each case  $\gamma_{\text{fiss}}$  increases rapidly toward higher chances, as the temperature of the fissioning nucleus decreases.<sup>21,23</sup> On the other hand, the chance distribution of  $\sigma_{\text{fiss}}$ , plotted in the lower part of the figure, changes dramatically from one parameter set to the next. A reduction in  $a_f/a_n$  leads to a greater fractional decrease in the corresponding ratio of level densities  $\rho_f/\rho_n$  at high than at low excitation energy, thereby suppressing low-chance relative to high-chance fission. A reduction

in  $C_f$  has a similar effect, leading to the greatest fractional increase in saddle-point intrinsic excitation, and hence in  $\rho_f/\rho_n$ , when the temperature is low. The two changes thus reinforce one another in suppressing low-chance and enhancing high-chance fission, while keeping the total fission cross section constant.

The overall observed anisotropy arises not from any single chance, but is rather weighted by the chance distribution for  $\sigma_{\text{fiss}}$ . Thus, as is clear from the table of mean  $\gamma_{\text{fiss}}$  results in Fig. 11, the progressive enhancement of high-chance fission as we go from parameter set *A* to *B* to *D*, in conjunction with the strong temperature dependence of  $\gamma_{\text{fiss}}$  for high chances, yields a rapid increase in the overall anisotropy. There is little change in the overall anisotropy between parameter sets *A* and *E* because the primary effect of the increases in  $a_f/a_n$  and in  $C_f$  from their RLDM-NIFG values is to further enhance the already dominant contributions from low chances, where  $\gamma_{\text{fiss}}$  varies only slowly with chance.

The results in Fig. 11 afford some insight into the likely effects on fission observables from shell corrections to the nuclear structure. Shell corrections, which may be important at the late chances (low temperatures), always tend to introduce modifications of *like sign* in deformation energies and corresponding level density parameters.<sup>19,26</sup> For example, if the late-chance decaying nuclides happen to fall near a shell closure at the saddle-point deformations, or in the middle of a shell at the equilibrium deformations, *both*  $C_f$  and  $a_f/a_n$  would be effectively lowered from RLDM-NIFG values. While the consequent effects on the level density at any one excitation energy tend to cancel one another, the cancellation is not complete—the energy dependence of the level density is modified. It is just this sort of alteration in the energy dependence which is reflected in the changes to the chance distribution and to  $\gamma_{\text{fiss}}$  in Fig. 11. (There is also a significant effect on the calculated variation of  $\sigma_{\text{fiss}}$  and  $\gamma_{\text{fiss}}$  with bombarding energy; see Refs. 6, 12, and 21.) The results in Fig. 11 suggest that while shell corrections to barrier heights and level density parameters may conceivably cancel in their effects on observed fission cross sections, it is unlikely for them to compensate simultaneously in *both*  $\sigma_{\text{fiss}}$  and  $\gamma_{\text{fiss}}$ . Thus, to the extent that the microscopic nuclear structure influences the decay properties observed in the present experiment, we may expect our RLDM-NIFG calculations to have difficulty in reproducing the measured target dependences of  $\sigma_{\text{fiss}}$  and  $\gamma_{\text{fiss}}$  simultaneously, since the compound

nuclei investigated here span a wide range in expected shell corrections<sup>2</sup> (e.g., from significant reductions in  $B_{\text{fiss}}$  in the Os region to increases in  $B_{\text{fiss}}$  near Pb).

There is one additional calculation (*C*) included in Fig. 11, this for a parameter set similar to *B*, but with the spin diffuseness parameter  $d_J$  from Eq. (9) increased substantially. This change has little effect on the chance distribution for  $\sigma_{\text{fiss}}$ , but significantly modifies the spin distribution (enhancing high-spin fission at the expense of low-spin fission, with a small decrease in  $a_f/a_n$  serving to keep the overall  $\sigma_{\text{fiss}}$  constant). The increase in  $d_J$  raises  $\gamma_{\text{fiss}}$  significantly, and nearly uniformly, at all chances. While for a given bombarding energy similar increases in  $\gamma_{\text{fiss}}$  may be caused by an increase in  $d_J$  or, alternatively, by decreases in  $C_f$  and  $a_f/a_n$ , the effect on the energy dependence of  $\gamma_{\text{fiss}}$  is different in the two cases.<sup>21</sup> As illustrated in Fig. 12,  $\sigma_{\text{fiss}}$  and  $\gamma_{\text{fiss}}$  are the only calculated quantities with significant sensitivity to  $d_J$ , both seeming to increase roughly as  $(d_J)^2$ . However, at the  $d_J$  values used in our master

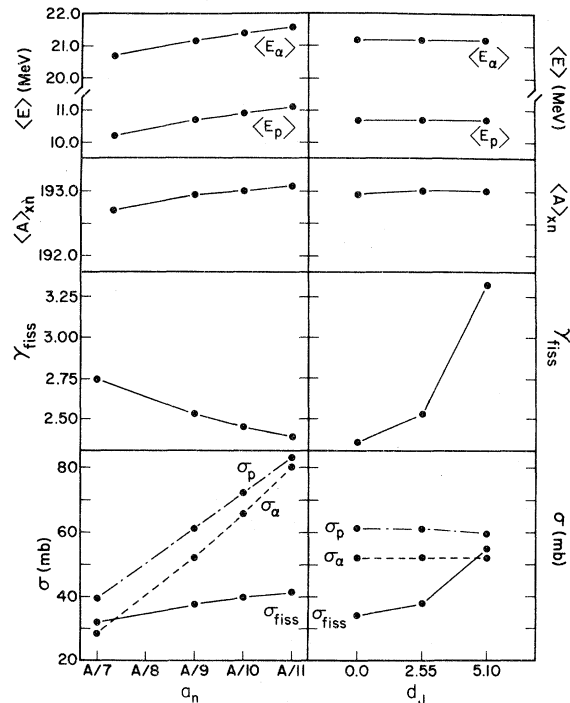


FIG. 12. Sensitivity of various calculated quantities for 74.8 MeV  ${}^6\text{Li} + {}^{194}\text{Pt}$  to the overall level density parameter  $a_n$  and to the diffuseness parameter  $d_J$  characterizing the initial compound-nucleus spin distribution. The quantities displayed in the top two frames are the mean kinetic energy  $\langle E \rangle$  of evaporated charged particles and the mean residue mass  $\langle A \rangle_{xn}$  reached in  $({}^6\text{Li}, xn)$  processes.

parameter set (see Sec. IV B), the deviations from calculations employing a sharp-cutoff spin distribution are not yet larger than the effects of 15% uncertainties in the measured absolute fusion cross sections.

In Fig. 12 we also illustrate the sensitivity of the calculations to the overall level density parameter  $a_n$  ( $=a_p=a_\alpha$ ). The major effect of varying  $a_n$  (and  $a_f$  proportionately) is to modify somewhat the rate of change of the level densities ( $\rho$ ) with excitation energy ( $U$ ). As  $a_n$  is reduced from  $A/7$  to  $A/11$ ,  $\partial\rho/\partial U$  decreases, favoring the evaporation of slightly higher energy particles. The small increases in mean proton and  $\alpha$  kinetic energies ( $\langle E_p \rangle$ ,  $\langle E_\alpha \rangle$ ) correspond to substantial increases in Coulomb barrier penetrability, and hence in  $\sigma_p$  and  $\sigma_\alpha$ . A similar small increase in  $\langle E_n \rangle$  (not shown in Fig. 12) has relatively little effect on the decay width  $\Gamma_n$ , but does lead to a small decrease in the mean number of neutrons emitted in  $({}^6\text{Li}, xn)$  reactions. The effects on  $\sigma_{\text{fiss}}$  and  $\gamma_{\text{fiss}}$  are small compared to their sensitivities to other parameters.

While the parameter variations considered in Figs. 10–12 are hardly exhaustive, they do serve to illustrate that the various calculated quantities we shall compare to experimental results are sensitive in quite different ways to the various statistical model input parameters. In Sec. V we shall note examples of other sensitivities useful in assessing the agreement between theory and experiment.

#### D. Effects omitted from the calculations

Our aim in the present analysis is to assess the degree to which the observed decay properties of hot, high-spin nuclei can be understood in a statistical model framework using simple macroscopic models for the relevant nuclear structure. In this context it is important to identify and correct (or at least estimate the uncertainties introduced by) shortcomings of conventional statistical model treatments, other than neglect of shell and pairing corrections to the structure. Several significant improvements to standard analyses are already incorporated in the calculations described in the preceding subsections. The most important remaining ambiguities in the treatment, associated with effects of preequilibrium particle emission and the expected disappearance of collective rotational bands at high excitation,<sup>22,23</sup> are addressed quantitatively in Secs. V B and V C, respectively. In the present section we mention a number of other effects which we have so far neglected in our calculations, along with at least qualitative reasons for expecting their influ-

ence to be small for the systems investigated here.

We have not included  $\gamma$ -decay competition with the particle emission and fission, as has been done in some other codes.<sup>7–9</sup> The  $\gamma$  competition is expected to become noticeable only at the very end of the decay chain, at excitation energies just above the neutron emission threshold; its only appreciable effect on our calculations might be to reduce very slightly the mean number of neutrons emitted in  $({}^6\text{Li}, xn)$  reactions. We have also omitted evaporation (or preequilibrium emission) of composite particles other than  $\alpha$ 's (e.g., deuterons and tritons, which together account for  $\sim 15\%$  of the measured  $\sigma_{Z=1}$ ); allowance for such cluster emission might slightly alter the calculated balance among the various particle decay modes and fission.

As already mentioned in Sec. IV B, we have neglected the effects of nuclear deformation on the barrier transmission coefficients for particle emission. Inclusion of such effects can lead to sizable enhancements of particle decay, especially the emission of  $\alpha$  particles or larger clusters, when the relevant deformations are large.<sup>47,49</sup> In the regions of interest here ( $A \simeq 200$ ,  $J \lesssim 40\hbar$ ) the enhancements would not be significant because the RLDM equilibrium deformations are quite small.<sup>1</sup> Indeed, in the following paper<sup>23</sup> (see also Sec. V C of the present paper) we find no more than 10% enhancement of  $\alpha$  decay when we apply an approximate treatment of the deformed potential barriers to hot nuclei with deformations substantially *larger* than the RLDM equilibrium values.

The small yrast deformations expected for these heavy nuclei are also likely to reduce to insignificance any practical consequences of the conceptual inconsistency<sup>50,51</sup> between the transition-state formalism applied to fission and the Hauser-Feshbach treatment of particle emission in the present, as well as most other, statistical model analyses. A more consistent transition-state approach to particle evaporation would evaluate the phase space for a configuration consisting of the ejectile just outside a residual nucleus with the same shape as the parent decaying nucleus, rather than for the configuration in which ejectile and equilibrium-deformed residual nucleus are at infinite separation.<sup>49–51</sup> However, one expects such an approach to yield results appreciably different from the present calculations only if the equilibrium deformations of the emitting and residual nuclei are quite different,<sup>49</sup> so that the particle decay must effect a large change in the nuclear shape.

As in most other statistical model codes, we have based our level density formalism on the approxi-

mation of a constant single-particle level density  $g_0$  in the vicinity of the Fermi energy  $\epsilon_F$ . A more exact NIFG treatment would include the variation of  $g$  with single-particle energy.<sup>52</sup> The resultant effect on our calculations would be small, since in all our applications the temperature  $\tau$  is small compared to  $\epsilon_F$ , and would probably be similar in nature to that arising from a small change in the overall level density parameter  $a_n$  (see Fig. 12): The rate of change of all level densities with excitation energy would be slightly modified, but with no significant direct influence on the ratio of level densities relevant to different decay modes.

The ratio of level density parameters  $a_f/a_n$  relevant to fission versus particle emission deviates from unity in a NIFG treatment because of the diffuse nuclear surface region and the deformation dependence of the surface-to-volume ratio.<sup>42</sup> While we have incorporated this effect to first order in our calculations by choosing for each system studied a single  $a_f/a_n$  value appropriate for a “typical” fissioning nucleus (see Sec. IV B), we have not explicitly included the variation of  $a_f/a_n$  (arising from variations in the RLDM saddle-point shape) with spin and chance. In the mass and spin region studied these variations are slow: Typically  $a_f/a_n$  decreases by 0.6–0.8% from the first-chance to the last-chance fissioning nuclide, and also from spin zero to the maximum angular momentum contributing appreciably to the calculated fission cross sections. The  $a_f/a_n$  values used in the present calculations fall in the middle of these ranges. The perturbations which would be introduced by the spin and chance dependences of  $a_f/a_n$  can be easily estimated from the calculated fission characteristics presented in Figs. 8–10: One should expect  $\sim 5\%$  increase in the calculated values of  $\sigma_{\text{fiss}}$  and perhaps  $\sim 1\%$  decrease in  $\gamma_{\text{fiss}}$ . It is much more crucial to include the spin dependence of  $a_f/a_n$  when one populates CN spins approaching the critical value at which  $B_{\text{fiss}}^{\text{RLDM}}$  vanishes ( $J_{\text{crit}} \sim 80\text{--}85\hbar$  in our cases), since in that limit the equilibrium and saddle-point deformations rapidly converge.

The diffuseness of the nuclear surface (and the finite range of the nuclear force) may be expected in general to modify RLDM predictions for the nuclear deformation energy, in addition to influencing level density parameters as described above. The modifications to some features of the RLDM structure predictions of Cohen, Plasil, and Swiatecki<sup>1</sup> have been considered by Krappe, Nix, and Sierk<sup>53</sup> and by Mustafa *et al.*<sup>54</sup> However, results from these improved treatments<sup>53,54</sup> are not yet available in sufficient detail (e.g., including the variation of

fission barrier heights, saddle-point shapes, and moments of inertia with  $N$ ,  $Z$ , and  $J$ ) for inclusion in our statistical model calculations. The neglect of these modifications does not have serious implications for the present work, since the structure calculations reported to date<sup>53,54</sup> indicate that for  $A \simeq 200$  there are at most very small ( $\leq 5\%$ ) differences from RLDM values for fission barrier heights and saddle-point shapes at zero angular momentum, and for critical angular momenta (where the fission barriers vanish). The differences are much larger for lighter compound nuclei and may explain at least part of the sizable reduction to RLDM fission barrier heights apparently needed to reproduce other fusion-fission measurements.<sup>6</sup>

It is also worth noting here several nonessential simplifying assumptions introduced in the calculations of the fission-fragment angular distribution  $W_{\text{fiss}}(\theta)$  in our code.<sup>21,23</sup> We assume that the angular momentum of the fissioning nucleus at its saddle point has zero projection along the beam direction ( $M=0$ ) and that the projection ( $K$ ) along the symmetry axis is characterized by a Gaussian probability distribution. As pointed out in the following paper,<sup>23</sup> these two approximations introduce small errors in  $\gamma_{\text{fiss}}$  which nearly cancel one another. We also neglect the “smearing” of the fragment angular distribution associated with multichance fission, which arises because prefission neutron emission introduces an angular spread of the decaying nuclei with respect to the beam direction. Inclusion of this effect would yield a reduction in the calculated values of  $\gamma_{\text{fiss}}$ , but only a very small one because most of the decaying nuclei in our cases must fall within  $\sim 5^\circ$  of the beam axis, and the derivative of  $W_{\text{fiss}}(\theta)$  is zero (or near zero) at the angles being compared in  $\gamma_{\text{fiss}}$ .

The neglect of all the above effects in the present version of our statistical model code, besides saving considerable computing time, serves mainly to increase *slightly* the theoretical uncertainties which should be attached to our pure RLDM-NIFG predictions. It is unlikely that inclusion of any of these effects would appreciably change the conclusions drawn from the present experiment and analysis.

## V. COMPARISON OF STATISTICAL MODEL CALCULATIONS AND EXPERIMENTAL RESULTS

### A. Equilibrium decay calculations

Measured and calculated fission cross sections and anisotropies are compared for five targets at

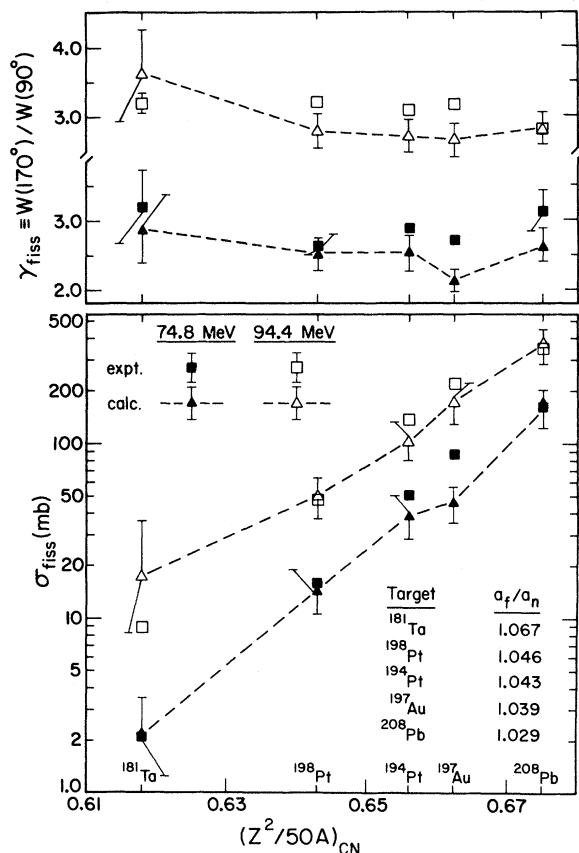


FIG. 13. Measured and calculated fission anisotropies and cross sections at two bombarding energies plotted versus the compound-nucleus fissility. The calculations use the master parameter set, including  $a_f/a_n$  values listed in the figure, and the individual measured fusion cross sections for each case. The error bars on the calculations arise from the measurement uncertainties in the total fusion cross sections. The dashed lines connect the calculated values.

two bombarding energies in Fig. 13. The results are plotted as a function of the fissility parameter<sup>1</sup>  $(Z^2/50A)$  for the CN. The calculations assume that the CN has reached complete thermal equilibrium prior to the first-chance decay. They use the master parameter set described in Sec. IV B (i.e., there are *no adjustable parameters*), and constrain the CN spin distribution to match the measured total fusion cross section appropriate to each target and energy. The absolute measurement uncertainty in  $\sigma_{\text{fus}}$  translates in our prescription into an uncertainty in the location of the cutoff in the CN spin distribution, i.e., in the parameter  $J_0$  in Eq. (9). These uncertainties in  $J_0$  (associated with the dashed  $\sigma_{\text{fus}}$  error bars in Fig. 7 and the errors in parentheses in Table I) are reflected in the error bars for the *calculated* points in Fig. 13, which are typically substan-

tially larger than the uncertainties in the corresponding measured quantities. Note, in particular, that the percentage error in each calculated value of  $\sigma_{\text{fiss}}$  is larger than the percentage error in  $\sigma_{\text{fus}}^{\text{meas}}$  from which it arises, because the partial width for fission varies rapidly with spin in the vicinity of  $J_0$ . Accurate absolute determination of  $\sigma_{\text{fus}}$  is thus essential to any meaningful comparison of statistical model calculations with fission measurements.

In light of the great sensitivity of  $\sigma_{\text{fiss}}$  and  $\gamma_{\text{fiss}}$  to statistical model parameters observed in Figs. 10–12, the overall agreement in Fig. 13 between the zero-adjustable-parameter calculations and measurements for both quantities is remarkably good, and unlikely to be fortuitous. The calculations for both  $\sigma_{\text{fiss}}$  and  $\gamma_{\text{fiss}}$  are in most cases very close to or slightly smaller than the experimental results; there are several exceptions to this trend, e.g., the 74.8 MeV results for  ${}^{197}\text{Au}$  and the 94.4 MeV results for  ${}^{181}\text{Ta}$ . However, if we refer back to Fig. 7, we see that the discrepancies in these two cases simply track with fluctuations in the measured total fusion cross sections. For this reason, it is of interest also

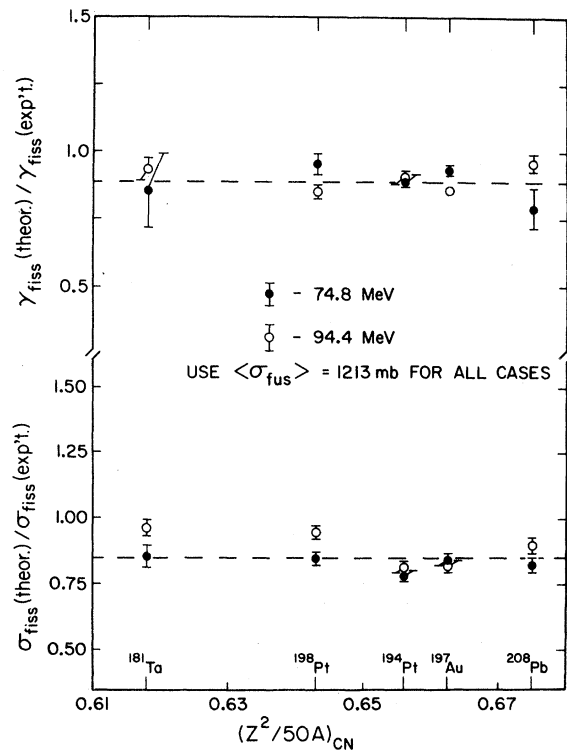


FIG. 14. The ratio of calculated to measured values of the fission cross section and anisotropy when the calculations employ the mean measured fusion cross section, rather than individual  $\sigma_{\text{fus}}$  results for each target and energy. The error bars represent only the relative measurement uncertainties in  $\sigma_{\text{fiss}}$  and  $\gamma_{\text{fiss}}$ .

to compare the measurements here to calculations in which the scatter in  $\sigma_{\text{fus}}^{\text{meas}}$  values is removed, i.e., in which the CN spin distribution is constrained in all cases to match the *average* measured fusion cross section  $\langle\sigma_{\text{fus}}\rangle = 1213$  mb, without including any associated uncertainty. The results of such a comparison are shown in Fig. 14 in terms of the ratio of predicted to measured values.

We find in Fig. 14 a remarkably accurate *quantitative* reproduction of the observed target dependence (and, over this admittedly small range of bombarding energies, of the energy dependence as well) of  $\sigma_{\text{fiss}}$  and  $\gamma_{\text{fiss}}$  by the statistical model calculations. This result is by no means trivial. We have included in these calculations, from the start, the variation of  $a_f/a_n$  with target nucleus (see the values listed in Fig. 13) arising from the deformation dependence of the single-particle level density for a NIFG confined by a potential with diffuse walls. If we had not included this effect (it has been neglected in most previous work), the  $\sigma_{\text{fiss}}$  points for  $^{181}\text{Ta}$  and  $^{208}\text{Pb}$  in Fig. 14 would differ from one another by a factor  $\simeq 3.5$ . If we had included the  $a_f/a_n$  variation and neglected only to calculate the initial CN excitation with respect to the liquid-drop, rather than the experimental, ground-state energy [i.e., if we had used the true fusion  $Q$  value in place of Eq. (7)], the  $\sigma_{\text{fiss}}$  points for  $^{181}\text{Ta}$  and  $^{198}\text{Pt}$  would differ from one another by  $\sim 30\%$ . In light of this strong sensitivity to small corrections in the statistical model input, the fact that we reproduce the observed target dependence of  $\sigma_{\text{fiss}}$  (and of  $\gamma_{\text{fiss}}$ ) to several percent without adjustable parameters is very significant.

Furthermore, the results in Fig. 14 present strong evidence that the effects of shell corrections on these overall fission characteristics are *negligible*. We have covered a range of compound nuclei over which the shell corrections at low spin are known, and those at high spin expected (e.g., see Ref. 2), to vary dramatically. We expect such shell corrections, if they are going to show up at all, to reveal themselves in target-dependent fluctuations of the theory-to-experiment ratios for  $\sigma_{\text{fiss}}$  and/or  $\gamma_{\text{fiss}}$  in Fig. 14, where the theory used has completely neglected microscopic structure contributions. Recall from our discussion of Fig. 11 that it is unlikely for the shell effects to cancel simultaneously in  $\sigma_{\text{fiss}}$  and  $\gamma_{\text{fiss}}$ . The absence of sizable fluctuations in Fig. 14 thus suggests that any shell corrections to the nuclear structure have indeed “melted” at the temperatures which dominate the observed fission decay. Such corrections, though undoubtedly present for *cold* nuclei in this mass region, apparently do

not yield a sufficient enhancement of high-chance fission contributions in any of the cases studied to affect the overall values of  $\sigma_{\text{fiss}}$  and  $\gamma_{\text{fiss}}$  significantly.

The results in Fig. 14 also reveal that the calculated absolute fission cross sections are systematically  $\sim 15\%$  low,<sup>55</sup> and the calculated anisotropies  $\sim 10\%$  low, in comparison with the measured values. These normalization discrepancies are very small in comparison with the variations which would arise from the range of adjustments to  $C_f$  and  $a_f/a_n$  considered in previous work. Indeed, the systematic deviations in Fig. 14 appear at this point to be of marginal significance, in that they could be accounted for by a plausible overall systematic error of  $\sim 10\%$  in the measured value of  $\langle\sigma_{\text{fus}}\rangle$ ; however, it pays to reserve judgement on the possible significance of the deviations until we have compared the calculations to other measured decay properties.

Since the target dependences of  $\sigma_{\text{fiss}}$  and  $\gamma_{\text{fiss}}$  are so well reproduced when we use the mean measured fusion cross section for all cases, we will continue to

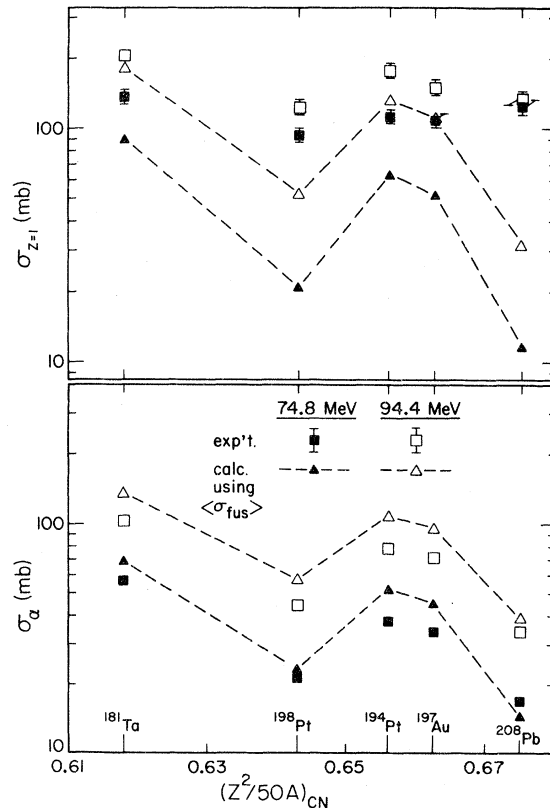


FIG. 15. Comparison of measured and calculated cross sections for  $Z=1$  and  $\alpha$ -particle emission, for five targets at two bombarding energies. The calculations use the master parameter set and the mean measured fusion cross section.

do so in the remaining comparisons of experiment and calculations. We thus effectively assume that the fluctuations in measured  $\sigma_{\text{fus}}$  values (see Fig. 7 and Table I) originate in the experiment, rather than in nature. (A possible, but less plausible, alternative explanation of the low  $\sigma_{\text{fus}}$  values for  ${}^{197}\text{Au}$  at 74.8 and 84.2 MeV, consistent with the observed fission results, would invoke a *lower* cutoff on the partial waves contributing to fusion with Au, appropriate to leave the upper spin cutoff  $J_0$  essentially the same as for the other targets.)

The calculations employing  $\langle\sigma_{\text{fus}}\rangle$  (without error bars) are compared with measurements of  $\sigma_\alpha$  and  $\sigma_{Z=1}$  in Fig. 15. For convenience the results are again plotted versus the CN fissility, although this is not an especially relevant parameter for the charged-particle decay. Let us address first the results for  $\sigma_\alpha$  in the lower frame. Here again we find the measured target dependence to be reproduced well, if not quite as precisely as for  $\sigma_{\text{fiss}}$  and  $\gamma_{\text{fiss}}$ , by our fixed-parameter calculations. The statistical model  $\alpha$ -evaporation cross sections tend, however, to be systematically higher, by  $\sim 30\%$ , than the experimental values.

Again, we might expect shell correction effects to alter the target dependence of  $\sigma_\alpha$  considerably, as illustrated in Fig. 16. In that figure we have plotted, for various assumptions concerning particle binding energies and level density parameters, the ratio  $\rho_\alpha(U_\alpha)/\rho_n(U_n)$  of intrinsic level densities relevant to the first-chance competition between evaporation of a 0.1-MeV  $s$ -wave neutron (reaching excitation energy  $U_n$  in the daughter nucleus) and of an  $s$ -wave  $\alpha$  particle with kinetic energy equal to the exit-channel Coulomb barrier height (reaching excitation  $U_\alpha$ ). When we use pure LDM binding energies and  $A/9.0$  for both  $a_n$  and  $a_\alpha$ , the target dependence of  $\rho_\alpha/\rho_n$  (see triangles in Fig. 16) closely reproduces that for  $\sigma_\alpha$  from the full calculations in Fig. 15, demonstrating that the essential ingredients affecting the calculated  $\sigma_\alpha$  are included in Fig. 16.

The three remaining sets of calculations in Fig. 16 represent the effects on  $\sigma_\alpha$  of including shell corrections to varying degrees. The closed circles result from calculations employing the known experimental (shell- and pairing-corrected) ground-state masses for the relevant nuclides, but still using  $A/9.0$  for level density parameters. The change from LDM particle binding energies leads to more pronounced fluctuations in  $\rho_\alpha/\rho_n$  with target nucleus, with a particularly striking enhancement for  ${}^{208}\text{Pb}$ , where  $\alpha$  decay leaves daughter nuclei close to the double shell closure at  $Z = 82$ ,  $N = 126$ . If shell

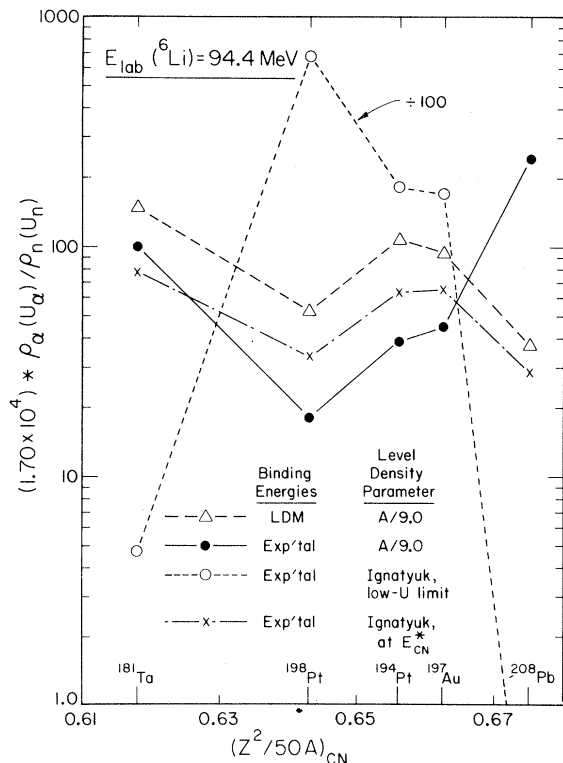


FIG. 16. Target dependence of the ratio  $\rho_\alpha(U_\alpha)/\rho_n(U_n)$  of intrinsic level densities relevant to first-chance  $\alpha$ - $n$  competition, calculated under various assumptions (see text) for the particle binding energies and level density parameters. The calculations illustrate the effects on  $\alpha$ -evaporation cross sections of including shell corrections to varying degrees in the nuclear structure parameters.

corrections are included also in the level density parameters, and are correlated with the mass corrections as appropriate for *cold* nuclei in the semiempirical prescription of Ignatyuk *et al.*,<sup>41</sup> then the target dependence of  $\rho_\alpha/\rho_n$  is yet much more pronounced (open circles in Fig. 16). Furthermore, the pattern is inverted from that produced by correcting only the binding energies, since the changes in  $a$  relevant to low excitation produce at high excitation a gross overcorrection for the shell effects on the masses. Finally, if we apply Ignatyuk's prescription<sup>41</sup> for the level density parameter at  $E_{\text{CN}}^*$ , rather than at low excitation, we nearly reproduce the LDM-NIFG results. This similarity (between the calculations represented by triangles and by crosses in Fig. 16) merely confirms that the level density prescription in Ref. 41 does the job it was intended to do: It includes a "melting" function specifically designed to phase out the shell corrections to level densities progressively with increasing excitation, so that they have nearly com-

pletely disappeared by the time we reach  $E_{CN}^*$ . The similarity of both calculations to the *observed* target dependence of  $\sigma_\alpha$  indicates that yet another aspect of the decay processes studied here can be understood without invoking significant shell effects.

Now let us return to the proton emission results in the upper frame of Fig. 15. Here we see the first major failure of our statistical model calculations. Neither the magnitude nor the target dependence of the observed  $\sigma_{Z=1}$  is adequately reproduced. In particular, there is a much weaker dependence on target and bombarding energy in the measurements than in the calculations. How can we do so well in understanding  $\sigma_{fiss}$ ,  $\gamma_{fiss}$ , and  $\sigma_\alpha$ , and so poorly for  $\sigma_{Z=1}$ ? The answer is contained in Fig. 17, where we compare calculated energy spectra for the evaporated particles with the spectra observed at  $\theta_{lab}=170^\circ$ . The calculated and measured spectrum shapes are in excellent agreement for  $\alpha$  particles. The calculated proton spectrum matches the obser-

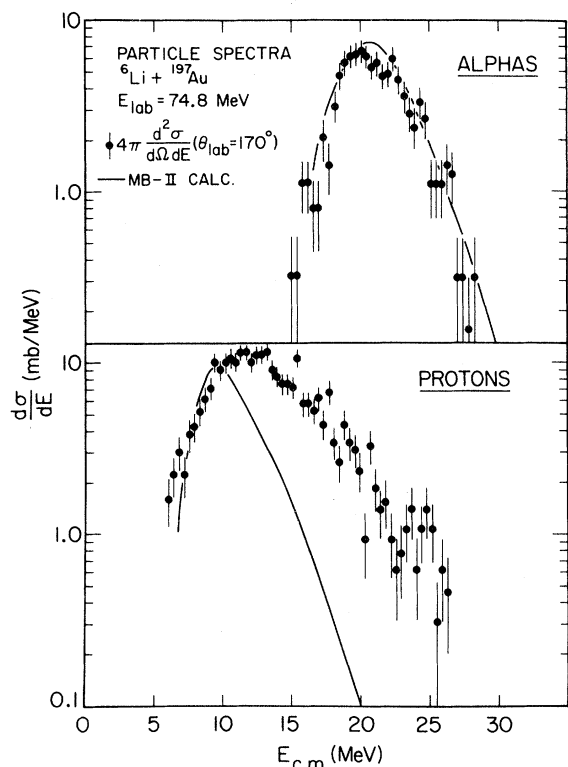


FIG. 17. Comparison of measured and calculated c.m. energy spectra for  $p$  and  $\alpha$  emission from 74.8 MeV  ${}^6\text{Li} + {}^{197}\text{Au}$  fusion. The measurements represent angle-integrated spectra inferred from the observations at  $\theta_{lab}=170^\circ$  under the assumption of isotropic emission. The measured spectra here have not been corrected to remove the small contributions associated with non-fusion reactions giving rise to energetic forward-going charged particles (see Sec. II E of text).

vations reasonably well at the low-energy end, but greatly underpredicts the yield of high-energy protons.

The location of the low-energy cutoffs in the charged-particle spectra are determined in the calculations almost exclusively by the barrier penetrabilities; our success in reproducing the relevant observations for both protons and alphas supports our earlier arguments (see Sec. IV B) in favor of the traditional optical model prescription for evaluating the  $T_v^l(\epsilon)$ . On the other hand, the high-energy tails in the evaporation spectra are sensitive primarily to the energy dependence of the level densities, i.e., to  $a_p$  and  $a_\alpha$ . There is simply no reasonable change in the nuclear structure which can account for the gross discrepancies at high proton energies in Fig. 17. Instead we interpret these discrepancies as evidence for surprisingly large yields of preequilibrium (PE) protons even at the most backward angles.

If we have evidence for substantial PE emission of protons, we must expect even larger PE yields of neutrons. These would show up in neutron energy spectra, which we have not measured, and in the distribution of ( ${}^6\text{Li}, xn$ ) residual nuclides, which we have determined from  $\gamma$ -singles spectra in a few cases. Experimental results for this distribution for 84.2 MeV  ${}^6\text{Li} + {}^{197}\text{Au}$  are compared in Fig. 18 with statistical model calculations. The observed distribution is shifted (by nearly one mass unit) toward higher-mass products, and is somewhat broader, than that predicted. These differences are con-

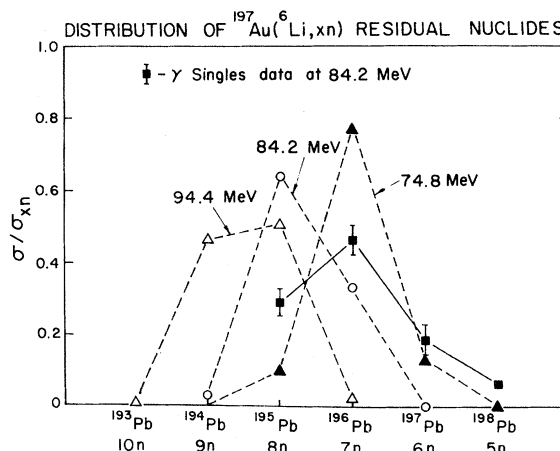


FIG. 18. The mass distribution of residual nuclides from  ${}^{197}\text{Au}({}^6\text{Li}, xn)$  reactions, as calculated at three bombarding energies and as deduced from  $\gamma$ -singles yields measured at 84.2 MeV. The fraction of the total ( ${}^6\text{Li}, xn$ ) cross section which goes into population of each isotope is plotted. The dashed lines connect the calculated values at each bombarding energy, while the solid lines connect the measurements.



sistent with the expected effects of PE emission, i.e., the emission of one or two neutrons during the decay chain with a broader spectrum of kinetic energies, and a significantly higher mean energy, than characterize evaporation.

While there is good evidence in Figs. 17 and 18 for substantial PE contributions to the observed decay processes, there are several associated features of the data whose origin we do not understand in detail. Why, for example, is the PE tail so pronounced in *back-angle* proton spectra, and the angular distribution deduced from back-angle measurements (Fig. 6) so flat? (The forward-angle cross sections in Fig. 6 may well be dominated by protons from various types of projectile fragmentation, which cannot easily be distinguished from PE protons at our bombarding energies.) These observations are consistent with a few previous calculations and measurements,<sup>56,57</sup> but seem inconsistent with others<sup>58-60</sup> and with much of the "folklore" built

up about PE phenomena. Why do we not see appreciable PE  $\alpha$  emission at large angles? Why would the back-angle PE proton cross section remain nearly constant in magnitude as a function of bombarding energy, as is suggested by the comparison of calculated and measured energy dependences in Fig. 19? (Note that for protons in Fig. 19 it is the absolute *difference* between experimental and theoretical cross sections which is constant, while for  $\sigma_\alpha$  and  $\sigma_{\text{fiss}}$  it is the corresponding *ratio*.) The available theories of PE phenomena<sup>56-60</sup> do not provide simple answers to these questions. For example, in the various thermodynamic models proposed,<sup>57,59</sup> the angular distribution of emitted nucleons results from some complicated interplay between the spatial and temporal variation of the nonequilibrium temperature field within the emitting nucleus, the reflection and refraction of the emitted particles upon passage through the nuclear surface, the rotation of the nucleus during equilibration, etc.

Despite all the detailed PE features which we do not understand, we have been able to develop a simple semiempirical prescription (described below) for *simulating* those essential features which are relevant to our predictions of fission and charged-particle evaporation characteristics. Incorporation of this prescription in our statistical model calculations will permit us to assess whether allowance for the PE contributions may adversely affect the good agreement found earlier with measurements of  $\sigma_{\text{fiss}}$ ,  $\gamma_{\text{fiss}}$ , and  $\sigma_\alpha$ .

### B. Effects of preequilibrium nucleon emission

It seems fair to assume that PE emission is confined to the early stages of the decay, before sufficient time for energy sharing among all degrees of freedom has elapsed. The excited nuclei produced in the early stages will then be characterized by significantly different excitation energy and spin distributions than those resulting purely from evaporation. It is these differences which will affect the probabilities for subsequent neutron and charged-particle evaporation and fission, and which are therefore important for us to simulate.

Our approach is based effectively on the existence of a "hot spot," occupying some fraction of the volume in the composite system, which is internally equilibrated at much higher temperature than the surrounding nuclear matter.<sup>57,59</sup> For calculations of the early-chance decays over some fraction of the

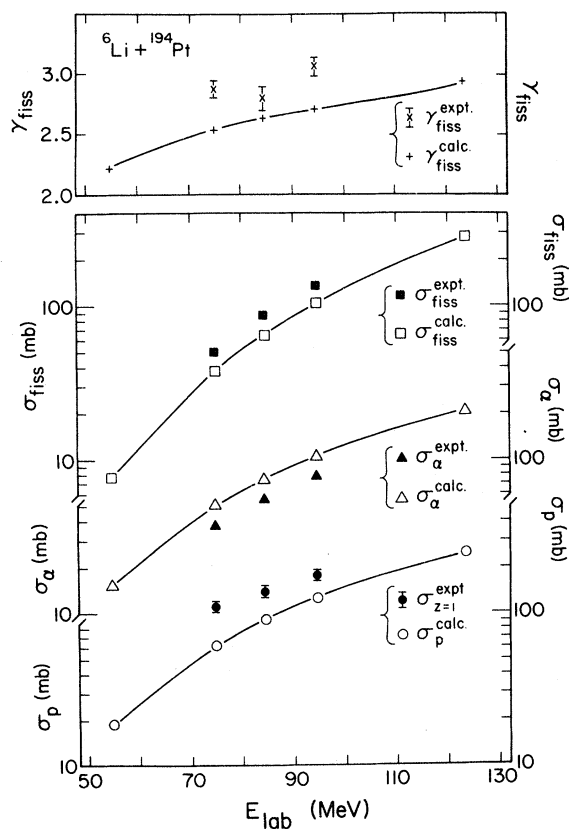


FIG. 19. Comparison of the calculated and measured energy dependences for  $\sigma_p$ ,  $\sigma_\alpha$ ,  $\sigma_{\text{fiss}}$ , and  $\gamma_{\text{fiss}}$  from  ${}^6\text{Li}$  bombardment of  ${}^{194}\text{Pt}$ . The calculations at 55 and 124 MeV are based on smooth extrapolations of the CN spin distribution from those used at the three intermediate energies.

initial CN spin distribution (corresponding to the “hot spot”), we allow  $n$  and  $p$  evaporation only, starting from an anomalously high nuclear temperature  $\tau_{\text{eff}}$ , chosen to guarantee emission of protons with the *observed* spectrum of energies. The high temperature is simulated by an artificial reduction in the level density parameters  $a_n = a_p$ . Except for this change we perform a standard equilibrium decay calculation, with the balance between  $n$  and  $p$  PE emission, and the angular momentum removed in the process, determined by the level densities  $\rho_\nu$  and the barrier transmission coefficients  $T_\nu^l(\epsilon)$ . After allowing this PE emission for the desired

number of chances (usually one or two), we revert to the original values of the level density parameters and evaluate the probabilities for the various modes of subsequent equilibrium decay using the  $E^*$ - $J$  population profiles resulting from the PE stage. The final decay cross sections calculated for this “hot-spot” region are then added to the results of a normal equilibrium calculation for the remaining fraction of the initial CN spin distribution.

In practice we determine the “hot-spot” temperature  $\tau_{\text{eff}}$  by fitting the high-energy portion of an observed proton spectrum with the following formula<sup>61</sup>:

$$\frac{d^2\sigma}{d\Omega_{\text{c.m.}}dE_{\text{c.m.}}}(\theta) \propto (E_p - 7 \text{ MeV}) \exp[-(E_p - 7 \text{ MeV})/\tau_{\text{eff}}], \quad (11)$$

where 7 MeV is the approximate proton kinetic energy at which Coulomb barrier impenetrability cuts the spectrum off. The value of  $\tau_{\text{eff}}$  deduced by fitting with Eq. (11) varies with the proton angle. We have taken  $\tau_{\text{eff}}$  from the observed spectrum at  $90^\circ$  as a suitable average value. (At  $170^\circ$ ,  $\tau_{\text{eff}}$  is 10% smaller than at  $90^\circ$ , while at forward angles it is presumably somewhat larger, but difficult to determine due to contamination of the spectrum with fragmentation protons.) The modified level density parameter  $a'_n$  is then chosen to make the *actual* intrinsic excitation energy  $U$  correspond to the anomalously high temperature  $\tau_{\text{eff}}$ :

$$U \simeq a\tau^2 \rightarrow a'_n = a_n(\tau_{\text{eq}}^2/\tau_{\text{eff}}^2), \quad (12)$$

where  $\tau_{\text{eq}}$  denotes the normal CN equilibrium temperature. The (“hot-spot”) fraction of the fusion cross section for which we use  $a'_n$  is adjusted to yield reasonable agreement with the measured distribution of ( ${}^6\text{Li}, xn$ ) residues. There is little experimental evidence on which to base some choice for the *location* of the “hot-spot” region in spin space. We have therefore performed calculations for various choices of this location, in order to investigate the range of possible effects on  $\sigma_{\text{fiss}}$ ,  $\gamma_{\text{fiss}}$ , and  $\sigma_\alpha$ .

While we explicitly calculate equilibrium decay widths following neutron emission in the PE stages, we feel justified (on the basis of Fig. 9 and the associated discussion) in neglecting contributions to overall fission and charged-particle evaporation cross sections which arise after the emission of PE (or evaporation) *protons*. Nonetheless, the PE proton emission can have a significant secondary effect, in that it renders some potentially important portion of the assumed initial spin distribution unavailable for fission. To include this effect, we impose a “self-consistency” requirement on the total

“fusion” cross section ( $\sigma_{\text{fus}}^{\text{PE}}$ ) used to constrain the spin distribution for the PE calculations:

$$\sigma_{\text{fus}}^{\text{PE}} = \langle \sigma_{\text{fus}}^{\text{meas}} \rangle + (\sigma_p^{\text{calc}} - \sigma_{Z=1}^{\text{meas}}). \quad (13)$$

The first term on the right is 1213 mb. The second term, typically  $\simeq 100$ –150 mb, represents that part of the total (PE plus evaporation) proton cross section *resulting* from the calculation in question which is not already included in  $\sigma_{Z=1}^{\text{meas}}$ .

The physical model implicit in the above prescription is undoubtedly oversimplified, and we do not expect it to explain all aspects of PE phenomena. For example, our calculations are intrinsically incapable of accounting for the fore-aft asymmetric angular distributions characteristic of PE particles, because we generate them strictly by an equilibrium decay from high temperature. Furthermore, the reduction in the energy derivative of the level densities which is required to account for the enhanced emission of energetic nucleons need not be attributed to a “hot spot” at all; rather, it may reflect limited access in the early stages of the decay only to some subset (associated with relatively simple particle-hole configurations<sup>58</sup>) of all the nuclear levels available at a given excitation. Nonetheless, our technique is quite adequate for our purposes of *simulating* the energy and angular momentum removal associated with PE emission and investigating the range of possible effects on subsequent equilibrium decay.

The results of calculations incorporating the above PE prescription are compared to those for an equilibrium calculation and to measurements for 84.2 MeV  ${}^6\text{Li} + {}^{197}\text{Au}$  in Fig. 20. Calculations for three different choices (labeled II, III, and IV) of the spin-space division between PE and equilibrium decay are included: In II, PE emission is allowed at

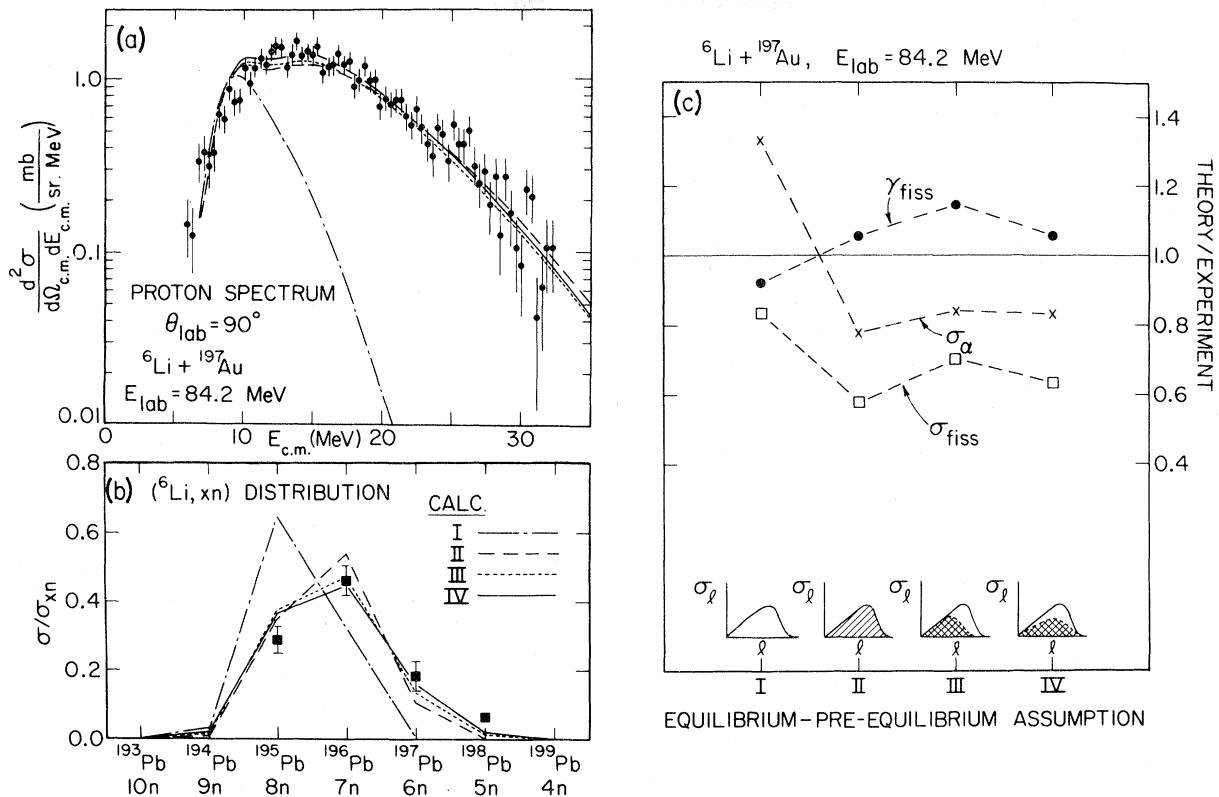


FIG. 20. Comparison of 84.2 MeV  ${}^6\text{Li} + {}^{197}\text{Au}$  measurements of (a) the  $90^\circ$  proton energy spectrum, (b) the distribution of  $({}^6\text{Li}, xn)$  residual nuclides, and (c) the fission cross section and anisotropy, and  $\alpha$ -evaporation cross section, with statistical model calculations based on four different assumptions concerning the competition between equilibrium and preequilibrium (PE) decay at the early stages. Calculation I assumes pure equilibrium decay for all spins and chances; II allows only PE emission of nucleons at the first chance, for all spins; III and IV allow PE emission at the first two chances from portions of the initial spin distribution, as represented by the cross-hatched areas in the  $\sigma_l$  vs  $l$  sketches in (c). In all cases the PE emission is assumed to occur from a "hot spot" of temperature  $\tau_{\text{eff}} = 4.8 \text{ MeV}$  (see Sec. V B).

the first chance only, but from the full spin distribution; in III and IV, two chances of PE emission are allowed from portions of the spin distribution, as sketched in Fig. 20(c). In all three cases  $\tau_{\text{eff}} = 4.8 \text{ MeV}$  is used for the PE stages of the decay. In parts (a) and (b) of the figure we see again that the normal equilibrium calculation (I) deviates widely from the observed proton spectrum and  $({}^6\text{Li}, xn)$  distribution. All three PE calculations reproduce these observables well, as they were constrained to do. [Actually, we have imposed a constraint only on the shape of the proton spectrum, not on the magnitude of the double differential cross section. The fact that the PE calculations reproduce this magnitude at the same time as the  $({}^6\text{Li}, xn)$  distribution suggests that the competition between PE proton and neutron emission is well treated.]

In Fig. 20(c) we have plotted the ratios of calculated to measured values for  $\sigma_{\text{fiss}}$ ,  $\gamma_{\text{fiss}}$ , and  $\sigma_{\alpha}$  for each of the four calculations. We see that inclusion

of the PE contributions reduces this ratio for  $\sigma_{\text{fiss}}$  and  $\sigma_{\alpha}$ , and increases it for  $\gamma_{\text{fiss}}$ . The directions of these changes are easily understood. Since we do not allow fission and  $\alpha$  evaporation to compete with the PE emission over the "hot spot" portion of the spin distribution (the fission fragments and back-angle  $\alpha$  particles we observe experimentally appear to come strictly from fully equilibrated nuclei), the cross sections for these processes at the first one or two chances are directly reduced. Their cross sections at subsequent chances are indirectly reduced since the mean temperature of the relevant decaying nuclei is lower than in a pure equilibrium calculation. (The mean spins of the decaying nuclei turn out to be no lower than in a pure equilibrium calculation, despite the somewhat greater average orbital angular momentum carried by the preequilibrium nucleons, because of the absence of fission competition at high spins during the PE phase.) Since the fission which survives comes from lower tempera-

tures,  $\gamma_{\text{fiss}}$  is increased relative to an equilibrium calculation. The small increase in extent of the initial spin distribution arising from Eq. (13) tends to add back a bit to  $\sigma_{\text{fiss}}$  and to increase  $\gamma_{\text{fiss}}$  further.

The quantitative PE effects seen in Fig. 20(c) are neither very large nor terribly sensitive to the number of PE chances or the spin-space location of the “hot spot,” so long as we constrain the calculations to reproduce the data in Fig. 20(a) and (b). Since, in addition, the observed features of the PE emission are quite similar for all the systems studied (e.g.,  $\tau_{\text{eff}}$  is nearly the same for all cases), we do not expect the PE effects to alter the calculated target dependences of  $\sigma_{\text{fiss}}$ ,  $\gamma_{\text{fiss}}$ , and  $\sigma_{\alpha}$  in any appreciable way. Our earlier conclusion concerning the negligible influence of shell corrections on these overall decay characteristics still stands. Only our estimates of the absolute deviations of theory from experiment have changed, with the calculations including PE effects now overestimating  $\gamma_{\text{fiss}}$  by a factor of 1.05–1.15, and underestimating  $\sigma_{\alpha}$  by a factor  $\simeq 0.8$  and  $\sigma_{\text{fiss}}$  by 0.6–0.7. The poorly known aspects of the PE emission appear to add  $\sim 10\%$  uncertainty to the other theoretical uncertainties (see Secs. IV D and V C, and Ref. 23) in the statistical model calculation of absolute values for these quantities. The remaining discrepancies between theory and experiment are somewhat larger and of a different nature than those which would arise from a conceivable error in the mean measured fusion cross section: e.g., increasing  $\langle\sigma_{\text{fus}}\rangle$  by 10% would typically lead to increases in  $\sigma_{\text{fiss}}$  by 15–20% and in  $\sigma_{\alpha}$  by 10% (making up less than half the discrepancies in Fig. 20), but would also increase  $\gamma_{\text{fiss}}$  by 5–10% (thereby worsening the corresponding discrepancy).

### C. Possible origins of the remaining discrepancies

The calculations incorporating PE nucleon emission in Fig. 20 employ only two adjustable parameters, the “hot-spot” temperature  $\tau_{\text{eff}}$  and the fraction of the fusion cross section to which  $\tau_{\text{eff}}$  is applied. These parameters have been adjusted to fit the observed 90° proton spectrum and ( ${}^6\text{Li}, xn$ ) residue mass distribution. All of the nuclear structure input parameters, specifically those with large direct influence on  $\sigma_{\text{fiss}}$ ,  $\gamma_{\text{fiss}}$ , and  $\sigma_{\alpha}$  (see Figs. 10–12), have been held fixed at the values predicted by the RLD and NIFG models (see Sec. IV B). The remaining quantitative discrepancies between calculations and measurements in Fig. 20(c) could

easily be removed if we were now to allow minor adjustments to some of the structure parameters. For example, suppose that we apply PE calculation IV from Fig. 20 (wherein 60% of the CN population at each angular momentum value yields PE nucleon emission at the first two chances), with  $\tau_{\text{eff}}=4.8$  MeV, to all target-bombarding energy combinations studied. We could then reproduce *all* measured fission cross sections and anisotropies to within  $\sim \pm 10\%$  by making a uniform 1–2% adjustment in the absolute values of  $a_f/a_n$  (maintaining the same target dependence indicated in Fig. 13) or, alternatively, by lowering all fission barrier heights by  $\sim 5\%$  (i.e., taking  $C_f \simeq 0.95$ ). These adjustments are very small in comparison with the ranges of “necessary” parameter variations claimed in previous fusion-fission analyses.<sup>5–14</sup> It does seem possible, in particular, for as much as a 5% reduction in RLD M fission barrier heights for  $A \simeq 200$  to be introduced by the diffuseness of the nuclear surface and the finite range of the nuclear force (see Refs. 53, 54, and Sec. IV D).

Modifications to  $a_f/a_n$  and/or  $C_f$  would not affect the calculated values of  $\sigma_{\alpha}$  (see Fig. 10). However, the remaining  $\sigma_{\alpha}$  discrepancy in Fig. 20(c) would disappear if we used  $A/9.9$ , rather than  $A/9.0$ , for the level density parameters relevant to particle emission. [It should also be kept in mind that in assuming an isotropic angular distribution for the  $\alpha$  evaporation (see Sec. II C) we may have slightly overestimated the *experimental* values of  $\sigma_{\alpha}$ .]

While we could thus produce an excellent fit to all of our measurements with only minor parameter adjustments, those adjustments would not be unique and would be of questionable significance. The magnitude of the remaining discrepancies is also comparable to the uncertainties we expect in our statistical model calculations from remaining theoretical inadequacies in our treatment of deformed-nucleus level densities and of preequilibrium effects, from our neglect of deformation effects on barrier transmission, and from a host of other, minor effects discussed in Sec. IV D.

We judge the most important omission from the calculations presented so far to be our neglect of the expected dilution of collective rotational band structure with increasing temperature. This effect is considered in detail in the following paper.<sup>23</sup> We conclude there that at the temperatures of interest in the present study, the collective enhancement of level densities is likely to be still fully effective at the highly deformed saddle points, but should already have disappeared at the relatively small

RLDM yrast deformations. The net result of this collective enhancement “fadeout” is to shift the daughter-nucleus shapes most probably reached in particle decay processes to deformations considerably larger than the RLDM yrast values. The extent of this shift increases with increasing temperature, and for fixed temperature with decreasing angular momentum of the daughter nucleus. Inclusion of the collective enhancement fadeout in the statistical model according to the prescription described in the following paper<sup>23</sup> leads necessarily to an increase in calculated values of  $\sigma_{\text{fiss}}$ , a decrease in  $\gamma_{\text{fiss}}$ , and an increase in  $\sigma_{\alpha}$  (resulting from the effect of the increased deformation on barrier transmission), in comparison with the calculations presented so far. All of these changes are in the ap-

propriate direction to improve the agreement between theory and experiment. The relative size of the effects on  $\sigma_{\text{fiss}}$ ,  $\gamma_{\text{fiss}}$ , and  $\sigma_{\alpha}$  is fixed by the fadeout prescription we have developed.<sup>23</sup> The treatment includes a single adjustable parameter ( $\zeta$ , of order unity) which scales the “cutoff” deformation for the collective bands, and hence determines the overall magnitude of the changes to calculated decay properties.

In Fig. 21 we compare the measured values of  $\sigma_{\alpha}$ ,  $\sigma_{\text{fiss}}$ , and  $\gamma_{\text{fiss}}$  for all five targets at  $E_{6\text{Li}} = 84.2$  MeV to calculations incorporating the collective enhancement fadeout in addition to PE emission at the early chances (calculation IV from Fig. 20,  $\tau_{\text{eff}} = 4.8$  MeV). The fadeout parameter  $\zeta$  has been adjusted to optimize the agreement for  $\sigma_{\text{fiss}}$  for  ${}^6\text{Li} + {}^{197}\text{Au}$ , and then held constant for all other cases. The resulting value  $\zeta = 1.05$  is physically reasonable.<sup>23</sup> The results in Figs. 20 and 21 demonstrate that with a total of three (nonstandard) adjustable parameters, we are able to reproduce all of the present experimental results quite well, specifically to  $\sim \pm 10\%$  for all quantities other than  $\sigma_{\alpha}$ . The enhancement of  $\sigma_{\alpha}$  from the collective fadeout and deformed barrier transmission is small ( $< 10\%$ ), and the calculated values continue to underpredict the measurements, generally by 10–20%. The  $\sigma_{\alpha}$  discrepancy for  ${}^6\text{Li} + {}^{208}\text{Pb}$  is worse, possibly reflecting very small residual microscopic corrections to the level densities at high excitation in the immediate vicinity of the (spherical) double shell closure at  $Z = 82$ ,  $N = 126$ .

The improved agreement between theory and experiment in Fig. 21 is encouraging, but cannot be viewed as clear confirmation for our somewhat speculative approach to incorporating the fadeout of collective bands.<sup>23</sup> Rather, we interpret the results of our most complete calculations as evidence that, *within current theoretical uncertainties in the statistical model treatment and experimental uncertainties in the determination of total fusion cross sections*, there is no need to alter simple RLDM-NIFG structure predictions *in any way* to understand the decay properties of the hot, high-spin nuclei investigated here.

## VI. CONCLUSIONS AND OUTLOOK

We have presented the results of a coherent program of measurements and statistical model analysis of decay properties of nuclei with  $A \simeq 200$  formed at high angular momentum and high excitation energy in  ${}^6\text{Li}$ -induced fusion reactions. Exten-

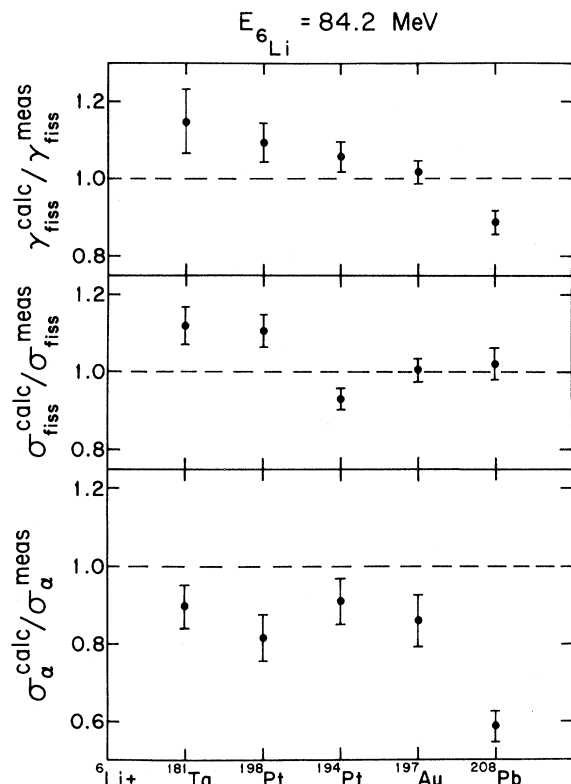


FIG. 21. The ratio of calculated to measured values of  $\sigma_{\alpha}$ ,  $\sigma_{\text{fiss}}$ , and  $\gamma_{\text{fiss}}$  for five targets at 84.2 MeV bombarding energy when the calculations include both pre-equilibrium nucleon emission (as in calculation IV of Fig. 20) and the fadeout of the collective level density enhancement with increasing temperature. The collective cutoff deformation scaling parameter  $\zeta$  (see Ref. 23) has been adjusted to the value 1.05 to optimize the agreement between calculated and measured values of  $\sigma_{\text{fiss}}$  for 84.2 MeV  ${}^6\text{Li} + {}^{197}\text{Au}$ . The error bars represent only the relative measurement uncertainties in  $\sigma_{\alpha}$ ,  $\sigma_{\text{fiss}}$ , and  $\gamma_{\text{fiss}}$ .

sive improvements to previous studies of high-spin fission have been incorporated in both the experiment and the analysis. Of particular importance is the measurement of a much wider variety of decay properties, for a number of nuclei spanning a narrow range in mass but a wide range of expected shapes and (low-temperature) shell effects. The statistical model calculations have been extended to include evaluation of fission-fragment angular distributions and an improved treatment of the level densities for deformed nuclei. We have considered quantitatively the effects on the calculations of preequilibrium particle emission, of the expected dilution of rotational band structure with increasing nuclear temperature, and of particle transmission through deformed potential barriers. A number of other possible shortcomings of the statistical model treatment have been discussed qualitatively and judged to have little significance for the systems investigated here. The input to the calculations has been constrained to as great a degree as possible, most notably by fixing *all* nuclear structure parameters to values consistent with the rotating-liquid-drop (RLD) and noninteracting Fermi-gas (NIFG) models (with care to include subtle effects which have often been neglected in the past, e.g., the deformation dependence of the NIFG level density parameter, and the use of the liquid-drop mass for the CN in computing the initial excitation energy). With this approach we have been able to test meaningfully the adequacy of the statistical model-RLD-NIFG treatment of the decay of hot, high-spin nuclei.

Our results demonstrate that the degree of constraint on the statistical model analysis improves greatly as a wider range of decay properties is considered, since different observables have quite different sensitivities to the various parameters of the calculations. For example: (i) the *combination* of  $\sigma_{\text{fiss}}$  and  $\gamma_{\text{fiss}}$  as a function of bombarding energy for a given target constrain  $C_f$ ,  $a_f/a_n$ , and the CN spin distribution; (ii) the target dependence of  $\sigma_{\text{fiss}}$  is especially sensitive to the non-negligible target dependence expected for  $a_f/a_n$ ; (iii)  $\sigma_\alpha$  is the cross section most sensitive to variations in the proportionality constant relating the overall level density parameter to mass number  $A$ ; (iv) the shapes of the back-angle proton and  $\alpha$ -particle spectra near the low-energy cutoffs are determined largely by the choice of prescription for the barrier transmission coefficients; (v) the high-energy part of the proton spectra and the mass distribution of ( ${}^6\text{Li}, xn$ ) residues exhibit clearly the effects of preequilibrium nucleon emission. All of the measurements play

significant roles in delineating our conclusions.

The most important conclusion from the present work is that the measurements of gross decay properties can be understood quite well using statistical model calculations based on pure RLDM-NIFG nuclear structure, so long as we allow for some preequilibrium (PE) nucleon emission at the early stages of the decay. Given the range of sensitivities mentioned above, the agreement is unlikely to be fortuitous. The accurate quantitative reproduction of the measured *target dependences* of  $\sigma_{\text{fiss}}$  and  $\gamma_{\text{fiss}}$ , and, to a slightly lesser extent, of  $\sigma_\alpha$ , is especially significant—it provides the clearest evidence we have that microscopic nuclear structure corrections, though undoubtedly present for cold nuclei, have little influence on the overall decay patterns for the hot, high-spin systems studied.

The effects of PE particle emission on subsequent equilibrium decay processes appear to be simulated adequately in our calculations by a “hot spot” approach employing two adjustable parameters, which are varied to fit measured proton energy spectra and ( ${}^6\text{Li}, xn$ ) residue mass distributions. Uncertainties  $\sim 10\%$  in the PE effects on  $\sigma_{\text{fiss}}$ ,  $\gamma_{\text{fiss}}$ , and  $\sigma_\alpha$  arise from our lack of knowledge about the variation of the PE emission probability with the angular momentum of the composite system. Allowing for these uncertainties, there still remain, after inclusion of the PE emission, appreciable overall normalization discrepancies between the calculated and measured absolute values for  $\sigma_{\text{fiss}}$ ,  $\gamma_{\text{fiss}}$ , and  $\sigma_\alpha$ . These discrepancies can be attributed, at least in part, to the fadeout with increasing temperature of the collective enhancement to level densities at the relatively mild deformations reached in particle decay. The quantitative extent of the collective enhancement fadeout effects, while it can be adjusted (via one parameter) to bring the calculations into reasonable agreement with all measured quantities, is not well constrained *a priori*,<sup>23</sup> since there is no independent information available on the degree of persistence of rotational bands at high excitation. Significant further improvements in the level of quantitative confidence one can place in statistical model calculations thus require a better understanding of level densities in deformed nuclei at high temperature and of the detailed mechanisms for preequilibrium particle decay.

At the present level of sophistication of the analysis, we can rule out the need for macroscopic or microscopic corrections of more than  $\sim 5\%$  to the nuclear structure input parameters. This result is in marked contrast to, although not necessarily inconsistent with, conclusions of fusion-fission

studies for lighter compound nuclei (e.g., see Refs. 6 and 12), where RLDM fission barrier heights have had to be reduced by as much as a factor of 2 to reproduce measurements. Calculated modifications to RLDM predictions<sup>53,54</sup> arising from the diffuseness of the nuclear surface and the finite range of the nuclear force are indeed sizable for  $A$  in the 100–150 region, but negligibly small for  $A \approx 200$ . In any case, we regard the conclusions of all earlier studies<sup>5–14</sup> as more questionable than those reported here, because previous workers applied less carefully constrained statistical model analyses to far less complete data sets. It would clearly be of interest to apply the guiding philosophy of the present work over wider ranges in mass and bombarding energy than we have investigated.

The success of the present statistical model analysis indicates that gross decay properties of hot fusion products are insensitive to microscopic structure corrections at high angular momentum but, at the same time, it serves to provide a credible signature for shell and pairing effects in more selective second-generation experiments. Specifically, one needs to develop experimental techniques for enhancing the decay contributions from *cold* nuclei; one would then expect microscopic structure corrections to introduce significant deviations of measured target dependences from those predicted by the statistical model-RLDM-NIFG calculations which succeed so well at high temperature.

There appear to be two basic methods for aiming future experiments more selectively at the decay of cold, high-spin nuclei. In the first, one would continue to form nuclei at high angular momentum and excitation in heavy-ion-induced fusion reactions, but would stress measurements with enhanced sensitivity to high-chance decay contributions. The fission anisotropy increases rapidly with decreasing temperature, and hence is already more sensitive to high-chance contributions than is  $\sigma_{\text{fiss}}$ . However, as an integral quantity (with contributions summed over all chances),  $\gamma_{\text{fiss}}$  would be most useful when the experimenter is lucky enough to choose for study nuclides where the microscopic structure corrections conspire to increase substantially the probability of late-chance fission. Crystal-blocking measurements, as reported in Ref. 9, are perhaps more generally useful, in that they allow one to separate (and map out the energy and target dependences for) short- and long-lifetime components of

fission, which are closely correlated with early- and late-chance events, respectively. Still more control (at still a greater expense of experimental effort) would be provided by a many-detector prefission neutron “multiplicity filter.”<sup>62</sup> (Prefission neutrons can be distinguished, in principle, from postfission neutrons since the latter have, and the former do not have, a significant angular correlation with the direction of the detected fission fragment.<sup>42</sup>) Such a device would allow one to emphasize fission from progressively lower temperatures by gating on higherfold neutron coincidences, just as in a  $\gamma$ -multiplicity experiment one can emphasize cascades from progressively higher spin by gating on higherfold  $\gamma$  events.

The second general method would involve the use of an appropriate *incomplete* fusion reaction to populate nuclei more selectively in the  $E^*$ - $J$  plane, namely, at relatively low  $E^*$  and high  $J$  (see Refs. 17 and 63–65). The entry region in the  $E^*$ - $J$  plane for the incompletely fused system could be adjusted experimentally by detecting the decay products in coincidence with the surviving projectile fragment, and simply gating on different energy bins for the latter particle. Ideally, one would like to scan entry regions from below to above the fission threshold in a given narrow spin range; in practice, it is probably difficult to reach low enough excitations in incomplete fusion while maintaining sufficient yield for a coincidence measurement. If one cannot “see” the fission threshold directly, but rather must still rely on a statistical model interpretation of such coincidence measurements, there is a significant worry: One has less guarantee of a statistical population of states in a relatively cold decaying nucleus when it is populated directly than when it is reached via multiple neutron evaporation from a hot CN. These two classes of second-generation experiments are thus complementary, and may both contribute to our further understanding of nuclear structure at high angular momentum.

#### ACKNOWLEDGMENTS

In several aspects of the experiments described herein, we received much appreciated technical assistance from Dr. D. L. Friesel. This work was supported in part by the U.S. National Science Foundation.

- \*On leave from Institute of Nuclear Research, 05-400 Swierk, Poland.
- †Present address: Bhabha Atomic Research Center, Bombay, India.
- ‡Present address: Institute for Nuclear Studies, Tokyo, Japan.
- <sup>1</sup>S. Cohen, F. Plasil, and W. J. Swiatecki, *Ann. Phys. (N.Y.)* **82**, 557 (1974).
- <sup>2</sup>G. Andersson, S. E. Larsson, G. Leander, P. Möller, S. G. Nilsson, I. Ragnarsson, S. Åberg, R. Bengtsson, J. Dudek, B. Nerlo-Pomorska, K. Pomorski, and Z. Szymański, *Nucl. Phys.* **A268**, 205 (1976).
- <sup>3</sup>K. Neergård, V. V. Pashkevich, and S. Frauendorf, *Nucl. Phys.* **A262**, 61 (1976); M. Faber, M. Ploszajczak, and A. Faessler, *ibid.* **A326**, 129 (1979); A. Ansari, O. Civitarese, and A. Faessler, *ibid.* **A334**, 93 (1980); A. Faessler, M. Ploszajczak, and K. W. Schmid, *Prog. Part. Nucl. Phys.* (to be published).
- <sup>4</sup>Proceedings of the International Symposium on High-Spin Phenomena in Nuclei, Argonne National Laboratory, 1979, ANL Report No. PHY-79-4, 1979 (unpublished).
- <sup>5</sup>M. Blann and F. Plasil, *Phys. Rev. Lett.* **29**, 303 (1972); F. Plasil and M. Blann, *Phys. Rev. C* **11**, 508 (1975).
- <sup>6</sup>M. Beckerman and M. Blann, *Phys. Rev. Lett.* **38**, 272 (1977); *Phys. Lett.* **68B**, 31 (1977); *Phys. Rev. C* **17**, 1615 (1978).
- <sup>7</sup>H. Delagrange, A. Fleury, and J. M. Alexander, *Phys. Rev. C* **16**, 706 (1977).
- <sup>8</sup>A. M. Zebelman, L. Kowalski, J. Miller, K. Beg, Y. Eyal, G. Yaffe, A. Kandil, and D. Logan, *Phys. Rev. C* **10**, 200 (1974).
- <sup>9</sup>H. Hagelund and A. S. Jensen, *Phys. Scr.* **15**, 225 (1977); J. U. Andersen, A. S. Jensen, K. Jørgensen, E. Laegsgaard, K. O. Nielsen, J. S. Forster, I. V. Mitchell, D. Ward, W. M. Gibson, and J. J. Cuomo, *K. Dan. Vidensk. Selsk. Mat. Fys. Medd.* **40**, No. 7 (1980).
- <sup>10</sup>T. Sikkeland, *Phys. Rev.* **135**, B669 (1964); T. Sikkeland, J. E. Clarkson, N. H. Steiger-Shafir, and V. E. Viola, Jr., *Phys. Rev. C* **3**, 329 (1971).
- <sup>11</sup>F. Plasil, *Proceedings of the International Conference on Reactions Between Complex Nuclei, Nashville, Tennessee, 1974*, edited by R. L. Robinson, F. K. McGowan, J. B. Ball, and J. H. Hamilton (North-Holland, Amsterdam, 1974), Vol. 2, p. 107.
- <sup>12</sup>F. Plasil, R. L. Ferguson, R. L. Hahn, F. E. Obenshain, F. Pleasonton, and G. R. Young, *Phys. Rev. Lett.* **45**, 333 (1980).
- <sup>13</sup>J. Bisplinghoff, A. Mignerey, M. Blann, P. David, and W. Scobel, *Phys. Rev. C* **16**, 1058 (1977).
- <sup>14</sup>F. Videbaek, R. B. Goldstein, L. Grodzins, S. G. Steadman, T. A. Belote, and J. D. Garrett, *Phys. Rev. C* **15**, 954 (1977).
- <sup>15</sup>M. Faber and M. Ploszajczak, *Z. Phys. A* **291**, 331 (1979).
- <sup>16</sup>S. E. Vigdor, D. G. Kovar, P. Sperr, J. Mahoney, A. Menchaca-Rocha, C. Olmer, and M. S. Zisman, *Phys. Rev. C* **20**, 2147 (1979); P. Gonthier, H. Ho, M. N. Namboodiri, L. Adler, J. B. Natowitz, S. Simon, K. Hagel, R. Terry, and A. Khodai, *Phys. Rev. Lett.* **44**, 1387 (1980).
- <sup>17</sup>K. Siwek-Wilczyńska, E. H. du Marchie van Voorthuysen, J. van Popta, R. H. Siemssen, and J. Wilczyński, *Phys. Rev. Lett.* **42**, 1599 (1979).
- <sup>18</sup>H. Delagrange, D. Logan, M. F. Rivet, M. Rajagopalan, J. M. Alexander, M. S. Zisman, M. Kaplan, and J. W. Ball, *Phys. Rev. Lett.* **43**, 1490 (1979).
- <sup>19</sup>R. Vandenbosch and J. R. Huizenga, *Nuclear Fission* (Academic, New York, 1973).
- <sup>20</sup>I. Halpern and V. M. Strutinsky, *Proceedings of the Second U. N. International Conference on Peaceful Uses of Atomic Energy* (United Nations, New York, 1959), Vol. 15, p. 408.
- <sup>21</sup>S. E. Vigdor, H. J. Karwowski, W. W. Jacobs, S. Kailas, P. P. Singh, F. Soga, and P. Yip, *Phys. Lett.* **90B**, 384 (1980).
- <sup>22</sup>S. Bjørnholm, A. Bohr, and B. R. Mottelson, *Proceedings of the Third International Symposium on the Physics and Chemistry of Fission, Rochester, 1973* (International Atomic Energy Agency, Vienna, 1974), Vol. I, p. 367.
- <sup>23</sup>S. E. Vigdor and H. J. Karwowski, *Phys. Rev. C* **26**, 1068 (1982), the following paper.
- <sup>24</sup>The properties of the PES can take on an effective dependence on excitation energy when one calculates nuclear level densities with an approximate formalism—such as that for a noninteracting Fermi gas, used in the present work—rather than from a combinatorial approach based on a realistic single-particle level spectrum; see Ref. 25.
- <sup>25</sup>L. G. Moretto, *Nucl. Phys.* **A182**, 641 (1972).
- <sup>26</sup>L. G. Moretto, *Proceedings of the Third International Symposium on the Physics and Chemistry of Fission, Rochester, 1973* (International Atomic Energy Agency, Vienna, 1974), Vol. I, p. 329.
- <sup>27</sup>A. Bohr and B. R. Mottelson, *Nuclear Structure* (Benjamin, New York, 1969), Vol. I, pp. 152–158, 281–293; *Nuclear Structure* (Benjamin, Reading, Massachusetts, 1975), Vol. II, pp. 591–636.
- <sup>28</sup>H. J. Karwowski, S. E. Vigdor, W. W. Jacobs, S. Kailas, P. P. Singh, F. Soga, and W. D. Ploughe, *Phys. Rev. Lett.* **42**, 1732 (1979); H. J. Karwowski, S. E. Vigdor, W. W. Jacobs, T. G. Throwe, D. L. Wark, S. Kailas, P. P. Singh, F. Soga, T. E. Ward, and J. Wiggins, *ibid.* **47**, 1251 (1981); *Phys. Rev. C* **25**, 1355 (1982).
- <sup>29</sup>S. E. Vigdor, *Nukleonika* (to be published).
- <sup>30</sup>M. Beckerman and M. Blann, University of Rochester Internal Report UR-NSRL-135, 1977 (unpublished).
- <sup>31</sup>P. Schwandt, W. W. Jacobs, M. D. Kaitchuck, P. P. Singh, W. D. Ploughe, F. D. Becchetti, and J. Jänecke, *Phys. Rev. C* **24**, 1522 (1981).
- <sup>32</sup>S. B. Kaufman, E. P. Steinberg, B. D. Wilkins, J. Unik, A. J. Gorski, and M. J. Fluss, *Nucl. Instrum. Methods* **115**, 47 (1974).
- <sup>33</sup>V. E. Viola, Jr., *Nucl. Data* **1**, 391 (1966).



- <sup>34</sup>C. M. Castaneda, H. A. Smith, Jr., P. P. Singh, and H. J. Karwowski, *Phys. Rev. C* **21**, 179 (1980).
- <sup>35</sup>B. Neumann, J. Buschmann, H. Klewe-Nebenius, H. Rebel, and H. J. Gils, *Nucl. Phys.* **A329**, 259 (1979).
- <sup>36</sup>Nearly isotropic particle evaporation is expected in the limit in which the evaporated particles remove little angular momentum from the emitting nucleus (e.g., see Ref. 44). The statistical model calculations presented in Secs. IV and V indicate that this is indeed the case for the present systems. The isotropy assumption is furthermore supported to within  $\sim 10\%$  by the angular distributions between  $90^\circ$  and  $170^\circ$  extracted for the lowest energy slices in the observed particle spectra.
- <sup>37</sup>G. Deconninck and N. Longequeue, *Phys. Rev. Lett.* **30**, 863 (1973); G. Deconninck and M. Longrée, *Phys. Rev. A* **16**, 1390 (1977).
- <sup>38</sup>H. Scofield, *Phys. Rev. A* **9**, 104 (1974).
- <sup>39</sup>The normalization against Rutherford scattering has also facilitated accurate determination of absolute ionization cross sections for atomic collisions producing target x rays; these results are reported in W. W. Jacobs, H. J. Karwowski, S. E. Vigdor, S. Kailas, P. P. Singh, F. Soga, and T. G. Throwe (unpublished).
- <sup>40</sup>N. Bohr and J. A. Wheeler, *Phys. Rev.* **56**, 426 (1939).
- <sup>41</sup>A. V. Ignatyuk, G. N. Smirenkin, and A. S. Tishin, *Yad. Fiz.* **21**, 485 (1975) [*Sov. J. Nucl. Phys.* **21**, 255 (1975)].
- <sup>42</sup>C. J. Bishop, I. Halpern, R. W. Shaw, Jr., and R. Vandebosch, *Nucl. Phys.* **A198**, 161 (1972).
- <sup>43</sup>M. A. McMahan and J. M. Alexander, *Phys. Rev. C* **21**, 1261 (1980).
- <sup>44</sup>T. Ericson, *Adv. Phys.* **9**, 425 (1960).
- <sup>45</sup>G. Sauer, H. Chandra, and U. Mosel, *Nucl. Phys.* **A264**, 221 (1976).
- <sup>46</sup>C. Y. Fu and F. G. Perey, *At. Data Nucl. Data Tables* **16**, 409 (1975); T. Mo and R. H. Davis, *Phys. Rev. C* **6**, 231 (1972); W. T. H. van Oers, H. Haw, N. E. Davison, A. Ingemarsson, B. Fagerstrom, and G. Tibell, *ibid.* **10**, 307 (1974); G. M. Hudson and R. H. Davis, *ibid.* **10**, 1521 (1974).
- <sup>47</sup>M. Beckerman and M. Blann, *Phys. Rev. Lett.* **42**, 156 (1979); M. Blann, *Phys. Lett.* **88B**, 5 (1979); *Phys. Rev. C* **21**, 1770 (1980).
- <sup>48</sup>When  $C_f \neq 1.0$  we assume that the saddle point—but not the yrast—line deviates from the RLDM values, and we simultaneously modify the saddle-point moment of inertia (needed in evaluating the level density and fission angular distribution) accordingly.
- <sup>49</sup>M. Blann and T. T. Komoto, *Phys. Rev. C* **24**, 426 (1981).
- <sup>50</sup>L. G. Moretto, *Phys. Lett.* **40B**, 185 (1972); *Nucl. Phys.* **A247**, 211 (1975).
- <sup>51</sup>R. G. Stokstad, in *Heavy Ion Science*, edited by D. A. Bromley (Plenum, New York) (to be published).
- <sup>52</sup>J. R. Huizenga and L. G. Moretto, *Annu. Rev. Nucl. Sci.* **22**, 427 (1972).
- <sup>53</sup>H. J. Krappe, J. R. Nix, and A. J. Sierk, *Phys. Rev. C* **20**, 992 (1979).
- <sup>54</sup>M. G. Mustafa, R. S. Newbury, P. A. Baisden, and H. Chandra, *Proceedings of the International Conference on Nuclear Physics, Berkeley, California, 1980*, edited by R. M. Diamond and J. O. Rasmussen (North-Holland, Amsterdam, 1981), abstract volume, p. 372.
- <sup>55</sup>The calculated fission cross sections in all cases are  $\sim 15\%$  higher than those reported in Ref. 29. This change results from correcting a long-standing, previously undiscovered error in the optical model subroutine TLJ used in particle evaporation calculations in the present, as well as a number of other, statistical model codes.
- <sup>56</sup>H. W. Bertini, R. T. Santoro, and O. W. Hermann, *Phys. Rev. C* **14**, 590 (1976).
- <sup>57</sup>S. I. A. Garpman, D. Sperber, and M. Zielińska-Pfabé, *Phys. Lett.* **90B**, 53 (1980).
- <sup>58</sup>M. Blann, *Annu. Rev. Nucl. Sci.* **25**, 123 (1975), and references therein.
- <sup>59</sup>R. Weiner and M. Weström, *Nucl. Phys.* **A286**, 282 (1977).
- <sup>60</sup>J. P. Bondorf, J. N. De, G. Fai, A. O. T. Karvinen, B. Jakobsson, and J. Randrup, *Nucl. Phys.* **A333**, 285 (1980).
- <sup>61</sup>L. Westerberg, D. G. Sarantites, D. C. Hensley, R. A. Dayras, M. L. Halbert, and J. H. Barker, *Phys. Rev. C* **18**, 796 (1978); H. Ejiri, T. Itahashi, Y. Nagai, T. Shibata, S. Nakayama, T. Kishimoto, K. Maeda, H. Sakai, and M. Hoshi, *Nucl. Phys.* **A305**, 167 (1978).
- <sup>62</sup>A. Gavron, J. R. Beene, B. Cheynis, R. L. Ferguson, F. E. Obenshain, F. Plasil, G. R. Young, G. A. Petitt, M. Jääskeläinen, D. G. Sarantites, and C. F. Maguire, *Phys. Rev. Lett.* **47**, 1255 (1981).
- <sup>63</sup>K. A. Geoffroy, D. G. Sarantites, M. L. Halbert, D. C. Hensley, R. A. Dayras, and J. H. Barker, *Phys. Rev. Lett.* **43**, 1303 (1979).
- <sup>64</sup>J. Wilczyński, K. Siwek-Wilczyńska, J. van Driel, S. Gonggrijp, D. C. J. M. Hageman, R. V. F. Janssens, J. Lukasiak, and R. H. Siemssen, *Phys. Rev. Lett.* **45**, 606 (1980).
- <sup>65</sup>An exotic form of incomplete fusion which might be particularly selective in populating cold, high-spin nuclei involves converting most of the excitation of the composite system into the production of a single pion of relatively low kinetic energy, which carries away almost no angular momentum. For a theoretical discussion of such "pionic fusion," see K. Klingenbeck, M. Dillig, and M. G. Huber, *Phys. Rev. Lett.* **47**, 1654 (1981).